Measurement of fragmentation cross sections of ^{12}C ions on a thin gold target with the FIRST apparatus

M. Toppi,[1] Z. Abou-Haidar,[2] C. Agodi,[3] M. A. G. Alvarez,[2] T. Aumann,[4] F. Balestra,[5,6] G. Battistoni,[7] A. Bocci,[2] T. T. Böhlen,[8] A. Boudard,[9] A. Brunetti,[10,11] M. Carpinelli,[10,11] R. Cirio,[5,12] G. A. P. Cirrone,[3] M. A. Cortes-Giraldo,[13] G. Cuttone,[3] M. De Napoli,[14] M. Durante,[4] J. P. Fernández-García,[13] Ch. Finck,[15] B. Golosio,[10,11] E. Iarocci,[1,16] F. Iazzi,[5,6] G. Ickert,[4] R. Introzzi,[5,6] D. Juliani,[15] J. Krimmer,[17] A. H. Kummali,[5,12] N. Kurz,[4] M. Labalme,[18] Y. Leifels,[4] A. Le Fèvre,[4] S. Leray,[9] F. Marchetto,[5] V. Monaco,[5,12] M. C. Morone,[19,20] D. Nicolosi,[21,3] P. Oliva,[10,11] A. Paoloni,[1] L. Piersanti,[22,16] R. Pleskac,[4] N. Randazzo,[14] R. Rescigno,[15] F. Romano,[3,23] D. Rossi,[4] V. Rosso,[24,25] M. Rousseau,[15] R. Sacchi,[5,26] P. Sala,[7] S. Salvador,[18] A. Sarti,[1,16,23,*] C. Scheidenberger,[4] C. Schuy,[4] A. Sciubba,[22,16,23] C. Sfienti,[3,27] H. Simon,[4] V. Sipala,[10,11] E. Spiriti,[1,28] S. Tropea,[3] M. Vanstalle,[15] H. Younis,[29] and V. Patera[22,16,23]

(The FIRST Collaboration)

[1]*Istituto Nazionale di Fisica Nucleare-Laboratori Nazionali di Frascati, Frascati, Italy*
[2]*Centro Nacional de Aceleradores (CNA), Universidad de Sevilla, Junta de Andalucía-CSIC 41092 Sevilla, Spain*
[3]*Istituto Nazionale di Fisica Nucleare-Laboratori Nazionali del Sud, Catania, Italy*
[4]*GSI Helmholtzzentrum fur Schwerionenforschung, Darmstadt, Germany*
[5]*Istituto Nazionale di Fisica Nucleare-Sezione di Torino, Torino, Italy*
[6]*Dipartimento di Fisica, Politecnico di Torino, Torino, Italy*
[7]*Istituto Nazionale di Fisica Nucleare-Sezione di Milano, Milano, Italy*
[8]*EBG MedAustron GmbH, Marie Curie-Straße 5, A-2700 Wiener Neustadt, Austria*
[9]*CEA-Saclay, IRFU/SPhN, Gif sur Yvette Cedex, France*
[10]*Istituto Nazionale di Fisica Nucleare-Sezione di Cagliari, Cagliari, Italy*
[11]*Università di Sassari, Sassari, Italy*
[12]*Dipartimento di Fisica, Università di Torino, Torino, Italy*
[13]*Departamento de Física Atómica, Molecular y Nuclear, University of Sevilla, 41080 Sevilla, Spain*
[14]*Istituto Nazionale di Fisica Nucleare-Sezione di Catania, Catania, Italy*
[15]*IPHC, Université de Strasbourg, CNRS, UMR7178, 67037 Strasbourg, France*
[16]*Dipartimento di Scienze di Base e Applicate per l'Ingegneria, "La Sapienza" Università di Roma, Roma, Italy*
[17]*IPN-Lyon, Universite de Lyon, Universite Lyon 1, CNRS/IN2P3, Villeurbanne, France*
[18]*LPC-Caen, ENSICAEN, Université de Caen, CNRS/IN2P3, Caen, France*
[19]*Istituto Nazionale di Fisica Nucleare-Sezione di Roma Tor Vergata, Roma, Italy*
[20]*Dipartimento di Biomedicina e Prevenzione, Università di Roma Tor Vergata, Roma, Italy*
[21]*Dipartimento di Fisica, Universitá di Catania, Catania, Italy*
[22]*Istituto Nazionale di Fisica Nucleare-Sezione di Roma 1, Roma, Italy*
[23]*Centro Studi e Ricerche e Museo Storico della Fisica "Enrico Fermi," Roma, Italy*
[24]*Dipartimento di Fisica, Universitá di Pisa, Pisa, Italy*
[25]*Istituto Nazionale di Fisica Nucleare-Sezione di Pisa, Pisa, Italy*
[26]*Dipartimento di Fisica, Universitá di Torino, Torino, Italy*
[27]*Medical Radiation Physics, Karolinska Institutet and Stockholm University, Stockholm, Sweden*
[28]*Istituto Nazionale di Fisica Nucleare-Sezione di Roma 3, Roma, Italy*
[29]*Department of Physics, COMSATS Institute of Information Technology, Islamabad, Pakistan*

(Received 18 November 2015; published 1 June 2016)

A detailed knowledge of the light ions interaction processes with matter is of great interest in basic and applied physics. As an example, particle therapy and space radioprotection require highly accurate fragmentation cross-section measurements to develop shielding materials and estimate acute and late health risks for manned missions in space and for treatment planning in particle therapy. The Fragmentation of Ions Relevant for Space and Therapy experiment at the Helmholtz Center for Heavy Ion research (GSI) was designed and built by an international collaboration from France, Germany, Italy, and Spain for studying the collisions of a ^{12}C ion beam with thin targets. The collaboration's main purpose is to provide the double-differential cross-section measurement of carbon-ion fragmentation at energies that are relevant for both tumor therapy and space radiation protection applications. Fragmentation cross sections of light ions impinging on a wide range of thin targets are also essential to validate the nuclear models implemented in MC simulations that, in such an energy range, fail to reproduce the data with the required accuracy. This paper presents the single differential carbon-ion fragmentation cross sections on a thin gold target, measured as a function of the fragment angle and kinetic energy in the forward

*Corresponding author: alessio.sarti@uniroma1.it

angular region ($\theta \lesssim 6^\circ$), aiming to provide useful data for the benchmarking of the simulation softwares used in light ions fragmentation applications. The ^{12}C ions used in the measurement were accelerated at the energy of 400 MeV/nucleon by the SIS (heavy ion synchrotron) GSI facility.

DOI: 10.1103/PhysRevC.93.064601

I. INTRODUCTION

Interest in the study of the mechanisms underlying the ion fragmentation in collisions at energies in the 10–1000 MeV/nucleon range has been constantly rising in the recent past, being driven by the possible use in space [1,2] and particle-therapy applications [3–5], where an improved description of the light-ion interactions with matter is eagerly needed.

Accurate measurements of fragmentation cross sections of light ions interacting with thin targets are also needed to benchmark and improve the nuclear interaction models implemented in Monte Carlo (MC) simulation algorithms. Nowadays, the disagreement between MC predictions and experimental data could be mainly ascribed to the lack of available data and their limited precision [5]. To provide an improved experimental to tune the MC simulations, a small set of measurements can be used: The interpolation of cross sections for different energies and target materials composition makes it possible, starting from a selected number of target-energy combinations, to build a model covering all the application needs.

In particular, for the cited applications, one of the most interesting ion-type–energy-range combinations to be explored is ^{12}C in the 200–1000 MeV/nucleon kinetic-energy range. As recently pointed out by NASA [6], cross-section measurements in this region using "a range of targets across the periodic table" are needed to provide the missing information in the nuclear fragmentation databases.

The ion fragmentation process has already been the object of several experimental campaigns in the past, aiming at either thin- or thick-target, single- or double-differential cross-section (DDCS) measurements [7–12]. Such measurements have been performed under different experimental conditions, covering in some cases only the very forward fragment emission region and in other cases a few other fixed-angle configurations. Recently a double-differential cross-section measurement in thin targets was performed using ^{12}C ions of 95 MeV/nucleon kinetic energy as projectiles, with an experimental setup able to cover a large angular range: 0° [13] and 4°–45° [14].

The principal aim of the Fragmentation of Ions Relevant for Space and Therapy (FIRST) Collaboration is to perform DDCS measurements using fully stripped ^{12}C ions as projectiles on thin targets in the energy range not yet covered by other experiments [15].

This paper presents the fragmentation cross section of 400 MeV/nucleon ^{12}C ions impinging on a thin gold target: a valuable input for the benchmarking of the nuclear models used for the description of the high-Z targets fragmentation. The data taking took place in the GSI laboratory (Darmstadt) in summer 2011 and about 5×10^6 events of collisions between a ^{12}C ion beam with a thin (500 μm thickness) gold target were recorded.

The experimental setup, which included a trigger counter, a beam monitor, a vertex pixel detector, a large-angle plastic scintillator compact detector, and a time-of-flight wall (TW) made of plastic scintillators, is fully described in Sec. II, together with the experiment data acquisition (DAQ) system. The performances obtained by the various subdetectors are outlined together with their calibration strategies and results.

Details on the data sample and on the Monte Carlo (MC) simulation are given in Sec. III, the description of the global reconstruction algorithms used to fully reconstruct all the fragments and particles traversing the detector in each event can be found in Sec. IV, while the results are presented in Sec. V. The studies performed to assess the systematic uncertainties are documented in Sec. VI, while the conclusions are presented in Sec. VII.

II. EXPERIMENTAL SETUP

Fragmentation cross sections are measured in FIRST using an experimental setup, already described in Ref. [15], that has been designed and optimized using a dedicated MC simulation. The schematic view of the FIRST experimental setup is shown in Fig. 1, together with the axis orientation of the reference frame.

The detection of the incoming ^{12}C ions has been accomplished by means of a start counter (SC), described in detail in Sec. II A, made of a thin layer of plastic scintillator whose geometry and readout were optimized to maximize the counting efficiency while keeping the pretarget fragmentation as low as possible. The SC was used to trigger the data acquisition using a minimum bias strategy: Whenever a ^{12}C ion was detected inside the SC the event was acquired. In addition, the SC provides the reference timing for time-of-flight measurements.

A pixel silicon detector (VTX), described in detail in Sec. II C, was placed just behind the target, allowing a precise reconstruction of the fragment tracks produced in the target and their angle with respect to the incoming beam direction, as well as their production vertex. The technology adopted for the vertex detector [16,17] made it possible to have the required efficiency with thin detection layers that minimized the out-of-target fragmentation of an elastically scattered ^{12}C ion or other fragments coming out from the target.

The long readout time (115 μs) of the pixel detector, with an incoming beam rate in the 1–10-kHz range, required the development of a dedicated fast beam monitor (BM) detector capable of resolving the event pileup (PU) ambiguity in the VTX by providing the position of the impinging ^{12}C ion in the target. The technology chosen and the performances of this detector are presented in Sec. II B.

A plastic scintillator compact detector (kinetic energy and time resolution optimized on scintillator, KENTROS) has been designed to detect fragments, mainly hydrogen and helium

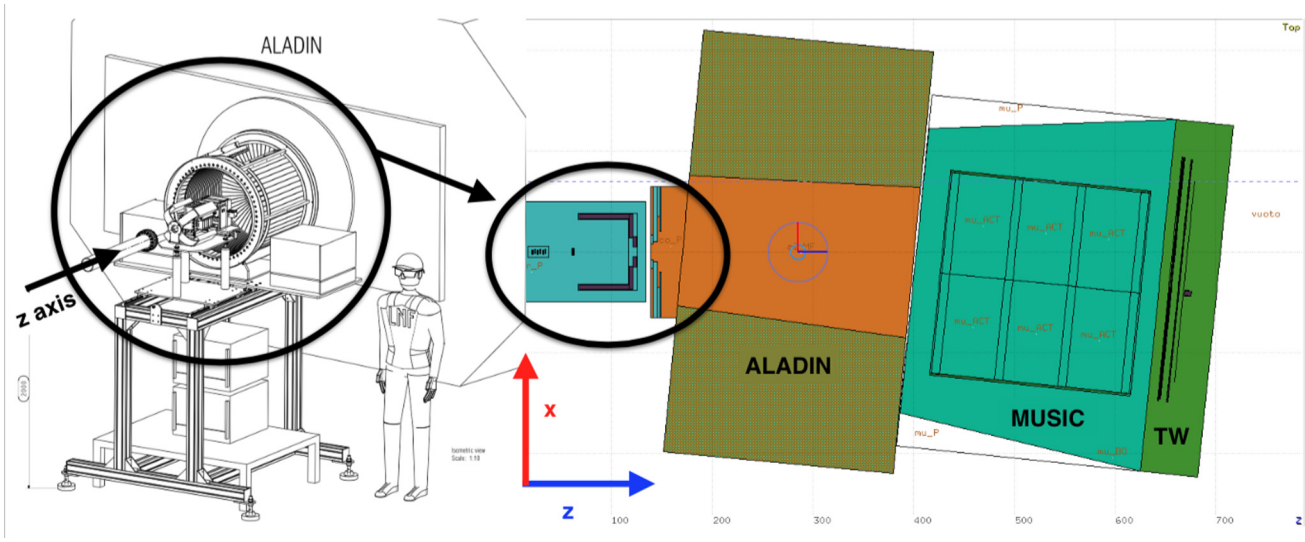

FIG. 1. (Left) Perspective view of the FIRST detector interaction region before the ALADIN magnet. The beam pipe after the last collimator and the beam exit window are shown with a black arrow superimposed, marking the beam direction (z axis). The SC surrounding the BM and KENTROS detector can be seen on top of the supporting table. (Right) Top view (x,z plane) of the FIRST experiment. From left to right: the table supporting the SC, the BM, and the VTX detectors, enclosing the target holder; the KENTROS detector, just before the magnet entrance window; the ALADIN magnet region; the TW detector at the rightmost position.

ions, emitted at large angles. This detector surrounds the target and vertex detector region covering the polar angle (defined as the angle between the incoming ^{12}C ion and the fragment direction) region between 6° and 90°. The results obtained in that region are not presented here and will be the subject of a dedicated paper in the future, where a fully detailed description of the detector technology will be published.

The charged fragment momentum is determined by measuring the bending of the trajectory in the z-x plane produced by the magnetic field provided by the large acceptance dipole magnet (ALADIN) magnet, whose description is reported in Sec. II D.

The fragment identification is performed using scintillating detectors placed 6 m away from the target region, arranged in a wall (TW), described in Sec. II E. Together with the time-of-flight (TOF) measurement, the TW provides the fragment coordinates and a measurement of the energy released inside the plastic scintillators: This information allows a clean separation of fragments with different charge.

An additional detector, a large-volume time projection chamber (TP-MUSIC IV [18]), was placed after the ALADIN magnet and before the TW, but could not be operated during the data taking: The full MC simulation of the experiment takes this detector into account to properly evaluate the material traversed by each fragment before reaching the TW and to account for possible secondary fragmentation.

A. Start counter detector

The SC detector, shown in Fig. 2, is used in FIRST to provide the measurement of the total number of ^{12}C ions used for the cross-section evaluation and the trigger signal for the data acquisition system. The SC also provides the reference time for all the other detectors, allowing the measurement of the drift time inside the BM and of the fragment TOF using the TW information. The detector consists of a 250-μm-thick plastic scintillator disk and the light is collected by 160 plastic optical fibers grouped into four bundles, each connected to a photomultiplier. The layout optimization, described in detail in Ref. [19], was hence performed carefully balancing the detector time resolution and the thickness minimization to have a pretarget particle interaction probability that is less than 1% with respect to the on-target one.

The efficiency [19] showed an excellent stability during the whole data taking, with a measured mean value of (99.7 ±

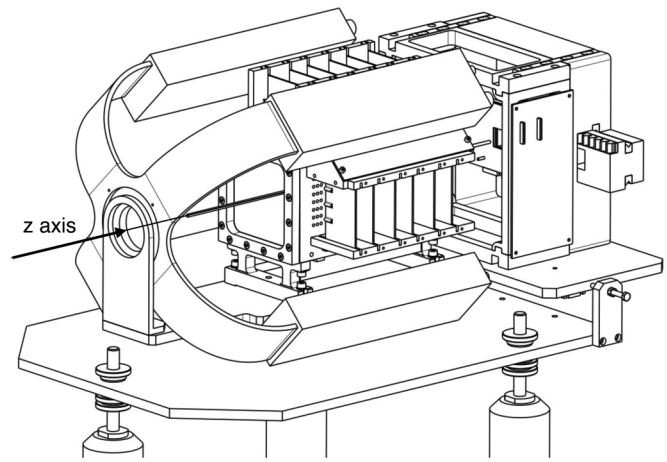

FIG. 2. Schematic view of the mechanical installation of the SC and BM detectors. The picture shows the BM, with six wire planes on both xz and yz views, encapsulated by the SC mechanical structure. The four arms of the SC, holding the fibers and the photomultiplier tubes used for the readout, can be clearly seen. The beam axis (z) is also shown, crossing the SC and the BM in the middle of their entrance windows. On the right, the aluminum box that encapsulates the target holder and the vertex detector is shown.

0.15)%. A good performance was also observed for the time resolution (σ_t), with a measured average value of $\sigma_t = (150 \pm 2)$ ps, where marginal fluctuations (maximum $\approx$5 ps) were observed.

B. Beam monitor detector

The BM, described in detail in Ref. [19] and shown in Fig. 2, is a drift chamber designed for the reconstruction of the charged-particle trajectory. This detector is used to measure the ion impinging point on the target, crucial information needed to resolve the PU ambiguity in the VTX detector (see Sec. II C 2).

The detector is made of 12 alternated horizontal (along the x axis) and vertical (along the y axis) wire planes. Each plane is composed of three rectangular cells centered around the sense wires, with dimensions $x\ (y) \times z = 16$ mm (16 mm) $\times$ 10 mm, for a total of 36 cells/sense wires. The geometrical layout has been optimized to minimize the ion interactions with the wires while still maintaining the required cell resolution. The 12 planes (6 on each "view") provide tracking redundancy and ensure a high tracking efficiency and an excellent spatial resolution. The BM was operated at 1.8 kV with an Ar/CO_2 (80%/20%) gas mixture at atmospheric pressure.

The detector tracking calibration has been performed using the tracks reconstructed in the VTX detector in a dedicated run in which the target was removed, thus allowing the detector alignment and the track intercalibration. Details of the tracking algorithms have been presented elsewhere [19].

The chamber hit detection efficiency was measured to be $\sim$97% and was stable during the data taking, as shown in Fig. 3 (black triangles): The largest run-by-run variations are within $\pm$3%. The mean track spatial resolution at the chamber center was measured to be $\sigma_x \approx 140$ μm, with the dependence on the distance from the cell center described in Ref. [19].

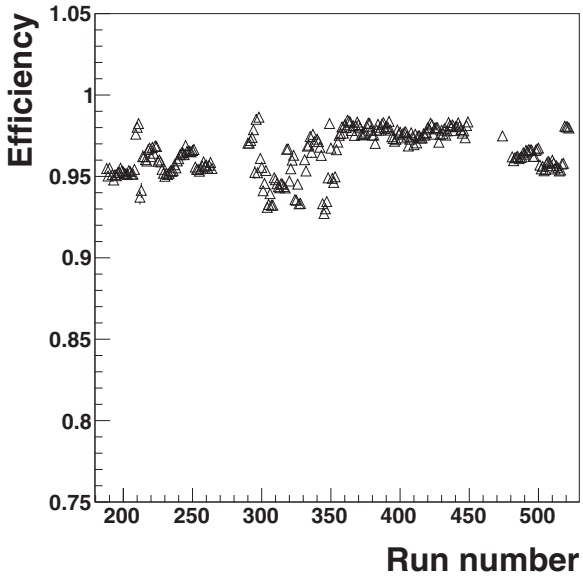

FIG. 3. BM tracking efficiency as a function of the run number. The small fluctuations ($\leqslant$3%) that can be observed against the mean value of 96.8% are attributable to the changes in the beam position, as well as to changes in the temperature and pressure of the gas mixture.

C. Vertex detector

The main purpose of the vertex detector (VTX) is the trajectory and fragmentation vertex reconstruction, with the largest possible angular coverage, of the fragments produced in the target.

The whole detector thickness should not exceed a few percent of the target thickness to keep the probability of fragmentation inside the sensors at a few percent level. A dynamic range from about two minimum ionizing particles (MIPs), for the proton signal to the two-orders-of-magnitude-larger signal from low-kinetic-energy ^{12}C ions has also to be considered. To satisfy those requirements, the MIMOSA26 (M26) pixel sensor has been chosen to equip the vertex detector with four sensor layers, corresponding to the best compromise between the need for having redundancy in the reconstruction and for minimizing the sensor total thickness.

M26 is a sensor chip developed by the Strasbourg group [16,17] for high-energy physics experiments. A sensitive area of 10.6 $\times$ 21.2 mm is covered by 576 rows and 1152 columns of pixels with 18.4-μm pitch. All the pixels are read out per column with a row readout time of 200 ns for a total readout time of 115.2 μs per frame. At the end of each column a discriminator is used to produce the input to the following zero suppression logic, which removes the empty pixel information and stores the data in two buffer memories. The data is sent off chip with two 80-MHz serial differential outputs. Only four discriminator thresholds, each common to 288 discriminators, are provided.

To fit the experimental conditions, a custom housing board has been designed with two M26 sensors glued on both sides of a square hole to obtain a sensitive area of $\sim 2 \times 2$ cm^2 including a small superposition region essential to align all the VTX sensors. The use of a 1-mm-thick printed circuit board (PCB) and low-profile components, allowing a distance of two consecutive boards of 2 mm, produces an overall thickness of the four vertex stations of 12 mm, as shown in Fig. 4. Under these conditions the angular coverage is $\pm 40^\circ$. Finally, the overall thickness of about 50 μm per sensor makes it possible to minimize the lateral straggling of the impinging particles.

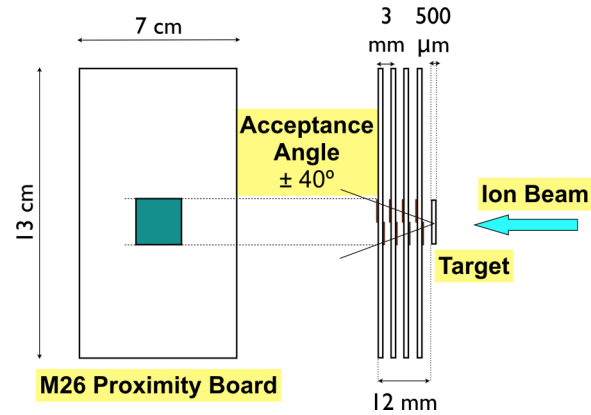

FIG. 4. Sketch of the VTX detector arrangement. The beam is impinging on the 500-μm-thick gold target. Each of the four following PCB planes is housing two sensors, one on each side, placed over a square hole (2 cm side length) in the PCB itself.

1. Performances

The VTX detector data processing starts from the raw data file reading, from which a list of fired pixels is extracted, and proceeds through the cluster reconstruction, centroid evaluation, and combination into a list of tracks and vertices. A clustering algorithm is used for each sensor to reconstruct the crossing point of the ionizing particles through the M26 sensor. The algorithm is based on a recursive method looking for the next neighboring fired pixel and is able to reconstruct correctly the clusters with an efficiency higher than 99.9% [20].

The tracking reconstruction is based on standard algorithms tuned for the specific applications of CMOS sensors aiming for the reconstruction of a track going from a given plane to the next. Starting from the last plane and proceeding backwards with respect to the beam direction, a path to the position given by the intersection of the BM track with the target is defined. Then all the available clusters on each plane within this path are identified and selected. The tracking reconstruction efficiency, evaluated on Monte Carlo simulation events (see Sec. III), is $98.7 \pm 0.1\%$, with a measured proportion of fake tracks of $1.99 \pm 0.01\%$ [20].

Two other different tracking approaches have been implemented and tested to assign a systematic uncertainty on the VTX tracking: One is based on the Hough transformation, while the other implements a different iterative procedure to scan the VTX planes to assign fired pixels to a given track in which consecutive planes are used. In the following, the first algorithm is used for track reconstruction because it is faster and exhibits a lower proportion of fake tracks.

The fragmentation vertex reconstruction is performed using an algorithm based on a probability distribution approach. Using the MC simulation a vertex reconstruction efficiency of $98.6 \pm 0.2\%$, with a $2.30 \pm 0.01\%$ proportion of fake vertices, has been estimated. The resolution of the vertex reconstruction, evaluated using Monte Carlo events, is better than 10 μm in the x and y directions and $\sim$50 μm in the z direction [20].

More than one ^{12}C ion can impinge on the VTX detector during the M26 sensor integration time (PU effect).

Using a Poisson distribution for PU events, with a λ parameter determined by data collected with the SC detector, it was found that only in $(2.4 \pm 0.1)\%$ of the events the vertex reconstruction algorithm could not disentangle the different vertices. From the data we obtain $\lambda = 0.63 \pm 0.12$, where the uncertainty comes from the distribution of the λ values for different data samples. More details about the performance of the VTX detector can be found in Ref. [20].

The VTX alignment procedure is based on the minimization of the distance between the reconstructed cluster centroid and the intersection of the reconstructed tracks on the sensor plane. The free parameters to be minimized are the displacement in the orthogonal plane with respect to the beam (x-y plane) and the rotation around the beam axis (z axis) for each sensor. Other rotations are neglected because the tracking procedure is less sensitive to them. The minimization is stopped once the variation of the displacement and angle is lower than a given value ($\Delta x, \Delta y < 5$ μm and angle $< 0.1^\circ$). Figure 5 shows the residuals obtained using straight tracks of ^{12}C ions at 400 MeV/nucleon for the x and y coordinates after the alignment procedure. The residuals are defined as the distance between the cluster positions and the fitted track line: Their distribution was used to evaluate the resolution of the tracking device given by the σ of a Gaussian fit. The resolution in x and y directions is better than $\sigma = 6$ μm and the fraction of tails outside a 4σ window is smaller than 13%.

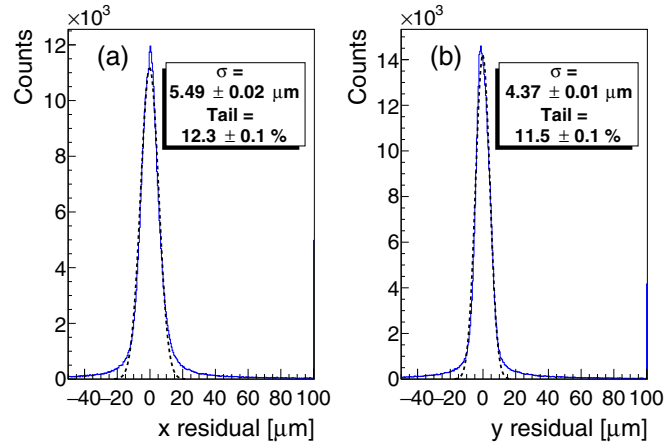

FIG. 5. The residuals obtained for the reconstructed tracks are shown in the x and y directions in the (a) and (b) images, respectively. In both plots the data distribution is shown in blue, while the result of a Gaussian fit to the histogram is superimposed as a black dashed line.

2. Matching with the BM

Because the tracks reconstructed by the VTX are the seed for the global track reconstruction algorithm (see Sec. IV), it is crucial to preselect the tracks that belong to each event, getting rid of the PU tracks that may have been reconstructed. The ambiguities on which tracks belong to the current event can be resolved by using the information from the BM track extrapolated to the target, because the BM readout time is fast enough to ensure that tracks belonging to different events cannot be mixed.

The track reconstructed in the BM is used to predict the impact point in the center of the target. The vertex positions reconstructed by the VTX for each event are compared with the carbon ion-target intersection point which is reconstructed by extrapolating the BM track. The closest vertex to the BM extrapolation is selected as a *matched vertex*. The impact of this selection on the final result and the relative systematic uncertainty on the cross section measurement is discussed in Sec. VI.

The BM and VTX detectors were software aligned using calibration events taken without any target, with tracks traversing both detectors without any fragmentation or scattering. The alignment constants were tuned by minimizing the distance between the two predicted track intersections with a virtual plane in the target position (VTX-BM residual distribution) and the difference between the track parameters (like the angle with respect to the beam axis θ). The alignment result is shown in Fig. 6, where a bias in the VTX-BM residual distribution smaller than 200 μm and a resolution of the order of 300 μm for the x coordinate are shown, with similar results for the y

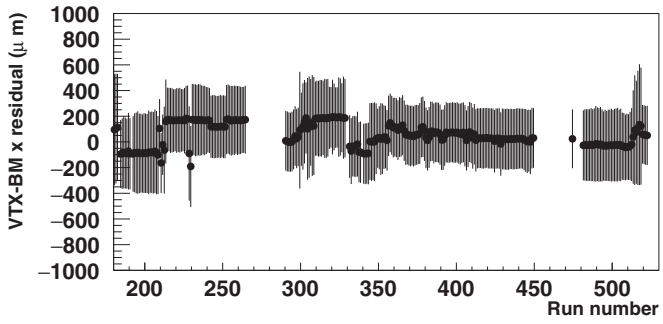

FIG. 6. Mean values of the residuals obtained for the x coordinate of ^{12}C ion tracks at the target position, as measured using the BM and VTX detectors. The error bars show the σ obtained from a fit done with a Gaussian probability density function (PDF) to the residual distribution and are consequently representing the detector matching resolution.

coordinate. Such results are compatible with the performances of the BM detector, reported in Ref. [19].

The ^{12}C ion beam has been monitored using both the VTX and BM detectors: A Gaussian-shaped beam spot has been observed during the data taking with a stable resolution ($\sim$1.3 mm) along both the x and the y axes.

D. ALADIN magnet

The p/Z ratio of charged fragments is reconstructed using the horizontal deflection (x-z plane) in the ALADIN. The magnetic field acts on the particles traveling in the magnet gap, operated in vacuum, that has an approximate volume of $155(H) \times 50(V) \times 230(L)$ cm^3. The magnet angular acceptance is limited to 5.7° by a circular collimator of 15 cm diameter positioned 75 cm from the target.

The value of the magnet current has been chosen so that a noninteracting beam particle crosses the central region of the TW, and it has been kept constant during the data taking within $\pm$0.5%. The corresponding deflection for a 400 MeV/nucleon ^{12}C ion is 5.3°.

The values of the magnetic field used in the reconstruction and simulation comes from the interpolation of maps measured at GSI along the three coordinate axes on about 10^4 grid points for different current values.

The actual current value used for the data analysis ($\sim$680 A, corresponding to a magnetic field of $\sim$0.55 T) is determined with the MC by requiring that a beam particle crosses the TW in the same positions as measured in special runs with and without the magnetic field. The uncertainty on the magnet current and field scale is limited by the TW position resolution and estimated to be 2.5%. The uncertainty on the field scale and on the position of the magnet with respect to the rest of the apparatus is taken into account in the evaluation of the cross-section measurement systematic errors.

E. TOF-wall detector

The TW detector has the aim of measuring the arrival time, the released energy, and the impinging positions of ions

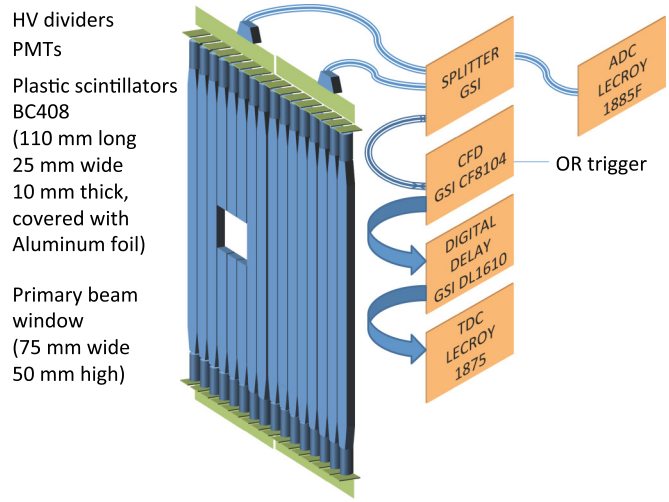

FIG. 7. Sketch of the TW scintillator modules and of the readout electronics with splitters, constant fraction discriminators (CFDs), digital delays, and TDC and ADC boards.

or fragments produced within the angular acceptance of the ALADIN entrance collimator.

Moreover, exploiting the information of energy release and arrival time, the TW allows the identification of the charge of each detected particle, from either the primary ^{12}C beam or the fragments. The detector, described in detail in Ref. [15], consists of two walls of BC-408 plastic scintillator slats (110 cm long, 1 cm thick, 2.5 cm wide) divided into 12 modules of eight slats each.

The detector is placed at a distance $d \simeq 600$ cm from the target, along the trajectory of the ^{12}C beam. The two walls are 8 cm from each other.

At the top and bottom ends of each slat, the signal of the crossing particle is read by two photomultiplier tubes. The output signals are split into two branches, as shown in Fig. 7. The first branch is read out by FASTBUS analog-to-digital converters (ADCs) for charge measurements. The second branch is processed by constant fraction discriminators (CFDs) and passes digital delay modules before entering time to digital converters (TDCs) that provide the time information.

1. TW calibration

As mentioned before, the TW detector is fundamental in the experiment layout because it measures the horizontal and vertical coordinates (x, y) of the impact point, the arrival time (TOF) and the energy released in the slats ($E_{\rm loss}$) of each detected particle. In particular, the coordinate in the horizontal plane is related to the slat number, which gives information on the x position of the particle and also on the fired wall (i.e., z coordinate).

The sum of the top and bottom TDC readings, which is independent of the hit position in the slat, is used to derive the particles' TOF. The ADC channel measurements, providing information on the collected charge, make it possible to calculate the energy ($E_{\rm loss}$) lost by the particle in the slat. $E_{\rm loss}$ is determined as the geometric mean of the upper and lower ADC values and it is independent of the fragment impact

position under the assumption of an exponential attenuation of the light in the scintillator.

The calibration of the quantities of interest have been performed exploiting particular data sets, called "sweep-runs," collected without a target, in which the beam conditions were known. In these runs the ^{12}C ion beam (at 400 MeV/nucleon) has been deflected on the horizontal plane over all the slats by varying the magnetic field. ^{12}C ions flew at known energy—and thus at known velocity—along paths which could be reconstructed by geometrical calculations. The hit coordinates (x,y,z), TOF, and $E_{\rm loss}$ are known, on average, for sweep-run hits: Delays, constant factors and gains can thus be calibrated comparing the measured quantities with the known values.

An additional data sample has been collected with dedicated runs to take into account the time dependence on the energy released by the fragments in each slat. A scan of the TW with the beam hitting an aluminum bar placed immediately before the scintillator front plane was performed. The time dependence on the released energy (time-walk effect) has been found to be $<$0.5 ns and thus it has been neglected in the TW hit reconstruction.

In calibration data samples, obtained scanning the TW with the primary C ions, the TOF is determined by the known energy (i.e., velocity) and the path length to the individual slats.

The fragment impact vertical position (y) can be obtained by using the ADC or TDC information, respectively. The first possibility is to calculate y through the ADCs ($y_{\rm ADC}$), assuming that an exponential attenuation is responsible for the signal decrease as a function of the length traversed along each slat and that the two photomultipliers can have different light gains. The calibration parameters have been measured by using the positions (y coordinates) of the intercept between the VTX track extrapolation and the TW planes as a reference.

The second possibility is, instead, to use the TDC readings and the light speed in the scintillator ($v_{\rm sl}$, slat dependent) to compute the y coordinate ($y_{\rm TDC}$). However, this latter method suffers from a bigger uncertainty in the position and is only used for slats in which only one ADC was working.

After the pedestal subtraction, the ADC readings can be related to the scintillation light released by the particle by knowing the attenuation and the gain of the photomultipliers for each slat.

In sweep runs the ^{12}C ion energy is known and the average energy loss can be evaluated according to the Bethe-Bloch formula. The computed $E_{\rm loss}$ is hence used to calibrate the TW detector parameters, taking also into account the nonlinear response of plastic scintillators to the ionization density by applying the semiempirical Birks' formula [21], with parameters that are determined from the data.

2. TW efficiency

The efficiency of the TW for hydrogen detection is limited by the minimum signal needed to trigger the CFDs and to digitize the time information in the TDCs.

To simulate accurately this effect, for each TW channel the fraction of events with a detected TDC hit is studied as a function of the ADC counts after pedestal subtraction. The minimum released energy needed to trigger the TDC in each channel is estimated using the calibration parameters and Birks' factors, and is used in the Monte Carlo simulation to discard hits with an energy below threshold.

The minimum TW energy that can be detected in at least one of the two TDCs depends on the threshold values and on the y position along the TW, owing to the light attenuation along the slats. The energy threshold is generally below the energy released by a minimum ionizing particle, with a few exceptions. These include specifically the region close to the impact point of the carbon beam, where higher thresholds are set and an efficiency loss for hydrogen ions of high kinetic energies is observed (a detailed discussion of the reconstruction efficiency can be found in Sec. IV C 3).

3. TW resolution

The resolutions in the TW reconstructed quantities ($E_{\rm loss}$, y, TOF) are estimated by comparing the values measured for hits in the two planes compatible with the same particle. The selection of the hits in different planes, optimized using the full Monte Carlo simulation, is based on the geometrical topology of the event and uses as input information the hit slat and y positions. The resolutions are used for the tuning of the Monte Carlo signal processing.

The $y_{\rm ADC}$ coordinate resolution was also evaluated using uncertainty propagation, obtaining similar results. The measured resolution, averaged on the whole detector for different slats and y positions, is shown in Fig. 8 (top left) as a function of the energy released in the scintillator by the fragment.

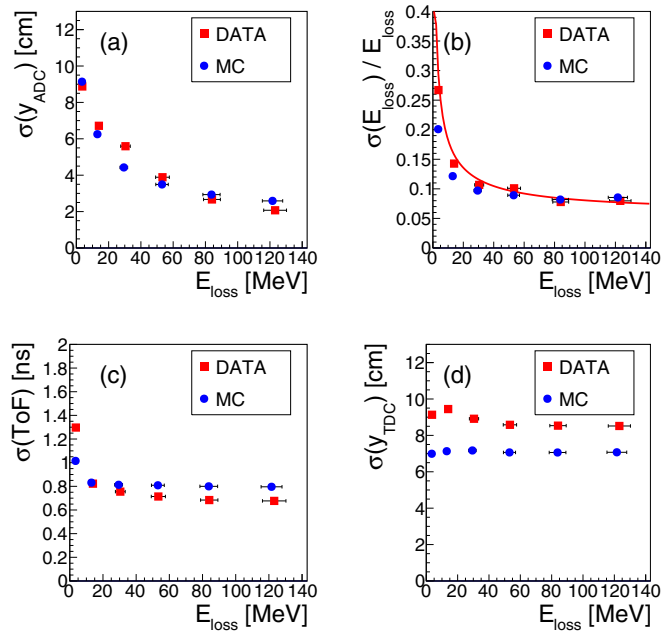

FIG. 8. The $y_{\rm ADC}$ resolution is shown in (a). The energy resolution is shown in (b). The TOF resolution is shown in (c). The $y_{\rm TDC}$ resolution is shown in (d). All the distributions are shown for data (red squares) and MC (blue circles) event samples as a function of the released energy. A red line, showing a $\propto 1/\sqrt{E_{\rm loss}}$ distribution is superimposed to the energy resolution distribution.

The energy resolution is shown in Fig. 8 (top right) for data and Monte Carlo as a function of the released energy. The TOF resolution, shown in Fig. 8 (bottom left), is about 800 ps, while the y_{TDC} resolution (bottom right) is 8 cm and is nearly independent of the energy.

F. Trigger and DAQ

The readout of the detector electronics is performed on an event-by-event basis using the multibranch system (MBS) [22], a general DAQ framework developed at GSI. For each trigger, the MBS system handles the readout of the bus controllers hosted in different crates and takes care of the trigger synchronization through signals distributed on a common trigger bus. The event fragments collected from all the individual controllers are transmitted during the beam interspill period to a host PC, where the data merging and saving is performed.

The signals from single detectors are locally processed with NIM electronics to generate trigger primitives. The final trigger logic is implemented in a FPGA programmable VME module (VULOM4 [23]), where the local trigger primitives are combined in logic matrices. The accepted triggers for different logical conditions are propagated to the readout electronics via the trigger bus. Different trigger outputs are generated with downscale factors or at random times for calibration purposes, while the main physical trigger is based only on the signal from the SC detector, thus providing an unbiased selection of primary beam particles for the data analysis.

The typical beam rate during the data taking was around 1 kHz, with instantaneous fluctuations related to the spill structures provided by the SIS. The mean acquisition rate was 150 Hz owing to the dead times of the single readout nodes.

III. DATA SAMPLE AND MC SIMULATION

The collected data sample of 400 MeV/nucleon ^{12}C ions collisions on a thin (500 μm thickness) gold target corresponds to 4.5×10^6 unbiased triggers.

The simulation of the experiment is based on the general-purpose Monte Carlo (MC) code FLUKA [24–26]. FLUKA includes sophisticated state-of-the-art models for nonelastic hadronic interactions and the successive deexcitation and radioactive decay of produced fragments. Two different MC samples have been produced using the FLUKA code. The first one was obtained simulating the interactions of 400 MeV/nucleon ^{12}C ions with a thin gold target and consists of 250×10^6 events. In the following we refer to this sample as the *full unbiased sample*. A second sample was produced to compute the kinetic-energy unfolding matrices and the tracking reconstruction efficiencies: In this sample the different fragments were generated with a flat energy and angular spectrum, originating from the target center. Ten million events of this kind were generated for each fragment type (Z number from one to five, most abundant isotopes). We refer to this sample in the following as to the *flat biased sample*.

The detector geometry and materials are modeled in considerable detail to properly evaluate the interactions in all the active detectors and the production of secondary particles in out-of-target fragmentation processes. The absolute positions of the detectors in the experimental area are fixed on the basis of the results of the optical survey measurement performed at the end of the data taking, complemented with alignment studies from the collected data.

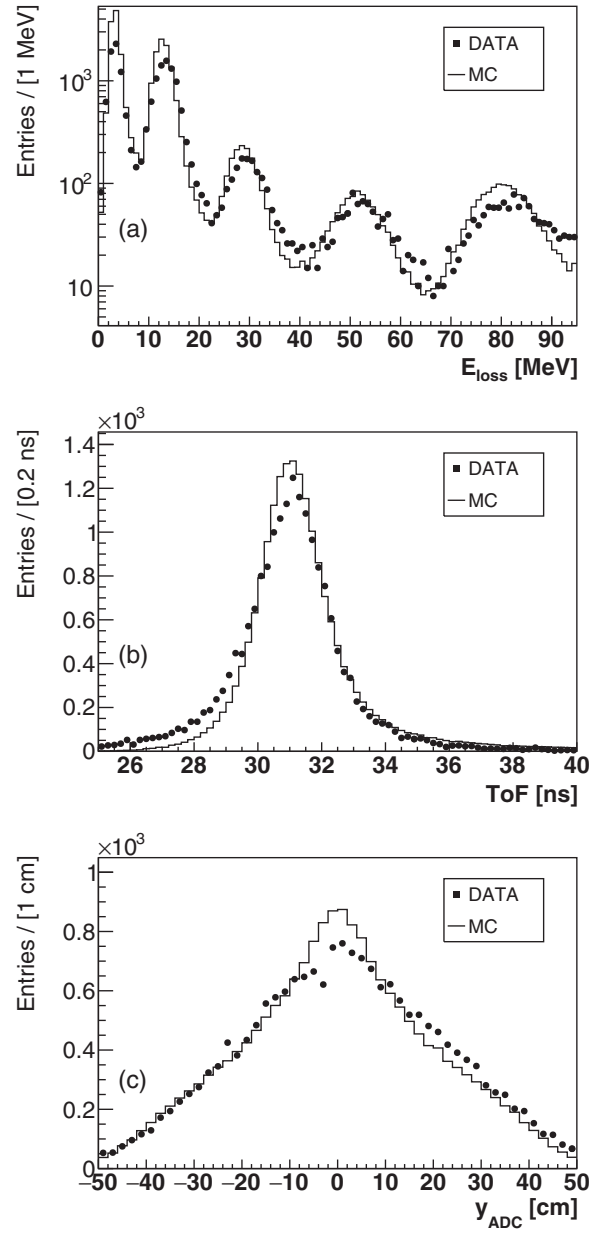

FIG. 9. Comparison of data and Monte Carlo distributions for TW reconstructed variables in fragmentation events. The data and MC spectra have been normalized to have the same integral. The E_{loss}, TOF, and y distributions are shown, respectively, in panels (a), (b), and (c).

The comparison of E_{loss}, TOF, and y coordinate measured from the TW detector for DATA and full unbiased MC events in which a fragmentation occurred are shown in Fig. 9, where the distributions have been normalized to have the same integral. The fragmentation events are defined as those in which at

least one vertex has been reconstructed in the VTX detector and more than one track is associated with it. The energy-loss distribution for data is shown up to 100 MeV for fragments with Z ranging from 1 to 5, because energy releases above 100 MeV are related to carbon ions. A detailed discussion on the charge identification of the fragments on the basis of energy loss and time of flight can be found in Sec. IV A.

The PU of VTX tracks from different primary particles is simulated by adding additional tracks from events stored in a software FIFO, according to a Poissonian distribution determined from the full data sample.

The detailed MC simulation of the geometry and of the detector response is needed to evaluate the acceptances and resolutions for the cross-section measurement. For this purpose each reconstructed track is associated with a MC-generated track and the reconstructed variables (kinetic energy, mass, charge, emission angle, momentum) are compared with the corresponding true value at generator level.

The full unbiased MC sample has been used to evaluate the tracking resolutions and to tune the combinatorial and misidentification background components subtraction in the mass spectra analysis (see Sec. IV C).

IV. GLOBAL RECONSTRUCTION

The fragment reconstruction in FIRST proceeds along two possible strategies, in accordance with their production angle: For small-angle production (polar angle θ less than $\sim 6^\circ$) the fragment enters the ALADIN magnet region, where the momentum is determined measuring the bending in the x-z plane, and is then detected by the TW; for large-angle production (θ larger than $\sim 6^\circ$), the fragment cannot enter the magnet region and hence are detected by the KENTROS detector.

The data analysis presented here covers only the small-angle production region: Fragments are reconstructed, in this case, using an iterative procedure providing the value of pc/Z and the trajectory path for each combination of VTX tracks and TW hits detected in the event. The selection strategy and the algorithms used to identify the right pairing of VTX tracks and TW hits from all the possible combinations is presented in Sec. IV B.

An example of a fully reconstructed fragmentation event, in which four fragments are produced at small angle, is shown in Fig. 10. The fired BM wires/cells are highlighted in blue in the grayish box in the bottom left corner of the picture. The KENTROS blue barrel and end-cap modules, surrounding the target-VTX region (not visible in this global view scale) are shown as well. The fragment tracks are represented as "dots" in space connecting the target origin position, and the relative four fragment tracks in the VTX, with the four pairs of red bands on the TW (two for each fragment as it traverses both the front and the rear wall) representing the TW slats that have been hit. The TW hits used to build the track are shown as tiny spots in green.

The track bending happens in the gray box, representing the ALADIN magnet region: Before and after that region the magnetic-field intensity is negligible and the track trajectory is assumed to be a straight line.

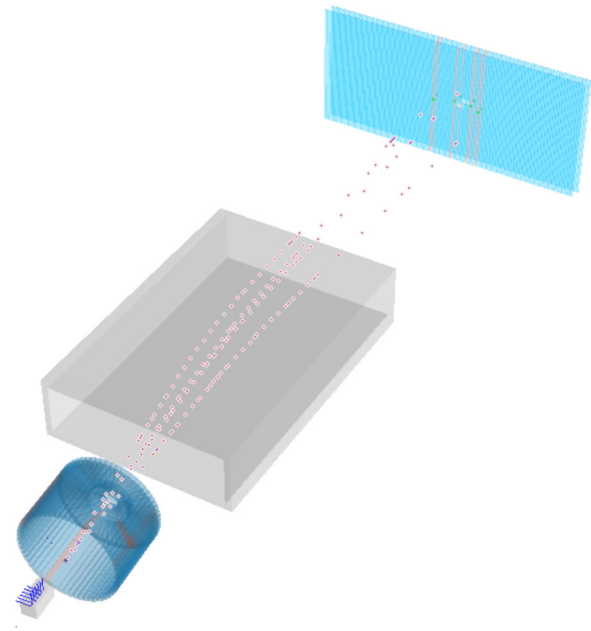

FIG. 10. Three-dimensional view of a fully reconstructed fragmentation event, with four fragments produced in the small-angle region. Fragment tracks are built by pairing tracks reconstructed in the VTX detector (not visible in this figure) with the hits detected by the TW (tiny green dots placed within the light pink lines, which identify the TW slats that have been hit in the top right light blue region representing the TW). The tracks are represented as dots connecting the target-VTX region with the green dots on the TW. The magnet region is represented as a gray box between the KENTROS detector and the TW.

A. Fragment charge identification

To compute the fragment momentum, the fragment charge (Z_{ID}) has to be measured. Two algorithms, based on the information from the TW and VTX detectors, have been developed.

The TW Z_{ID} identification is performed using the E_{loss} and TOF measurements. The TW resolution allows the discrimination of six spots in the E_{loss}-TOF plane, related to different fragment charges as shown in Fig. 11. The Bethe-Bloch formula parameters, used to describe the measured E_{loss} vs TOF of the ions with different Z, were experimentally tuned by means of a fit to the E_{loss} vs TOF projection to achieve the best description of the data. Figure 11 shows the measured distributions for ^{12}C ions on carbon target data, with fitted Bethe-Bloch curves superimposed in black.

The TW Z_{ID} algorithm assigns to a given fragment the charge that minimizes its normalized distance, in the E_{loss}-TOF plane, with respect to the different Bethe-Bloch curves relative to the different Z hypothesis. The normalized distance $[(\mathrm{dist} - \mu_{\mathrm{dist}})/\sigma_{\mathrm{dist}}]$ is computed, for each Z hypothesis, using the mean (μ_{dist}) and the σ (σ_{dist}) evaluated from a Gaussian fit to the distance of each hit to each Bethe-Bloch curve, in the full data sample.

The VTX detector identification algorithm exploits the correlation between the size of the hit clusters and the fragment charge, as outlined in Ref. [27].

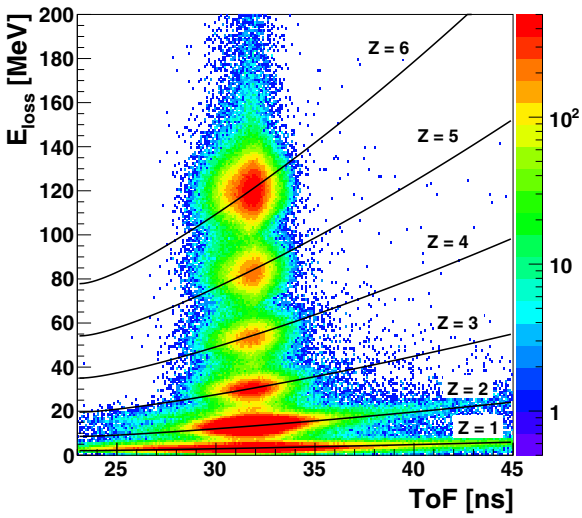

FIG. 11. Measured E_{loss} vs TOF distribution, for all the TW hits reconstructed in the full data sample. The corresponding Bethe-Bloch curves, with parameters tuned to reproduce the observed data sample distribution, are superimposed in black.

The VTX Z_{ID} algorithm has been calibrated on data, using the measured mean cluster size (number of pixels in the cluster) for a given VTX track, as a function of the Z_{ID} measured with the TW detector on a pure sample of global tracks identified applying tight selection cuts. The correlation between these two quantities is shown in Fig. 12.

For each reconstructed track, the VTX Z_{ID} algorithm compares the mean cluster size along the track with the calibrated distributions to assign a probability for each Z hypothesis. The hypothesis with the largest probability is then used to assign the Z_{ID} to the fragment.

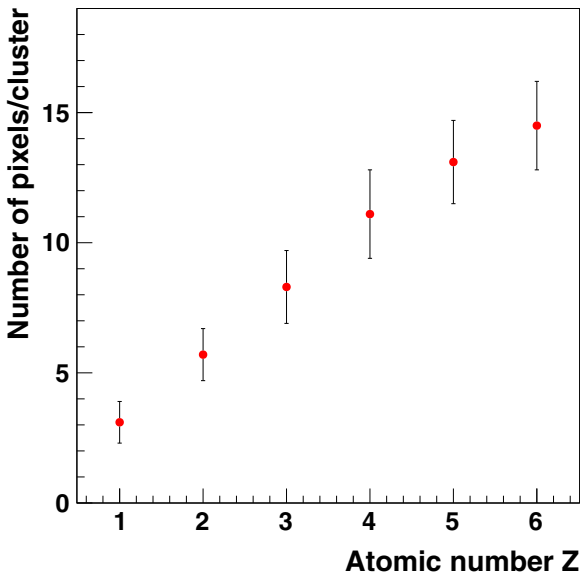

FIG. 12. VTX tracks mean cluster size (number of pixels per cluster) as a function of the fragment charge assigned from the TW Z_{ID} algorithm in a clean sample of global reconstructed tracks.

B. The global tracking algorithm

The global tracking algorithm implements three main steps.

(1) The events are preselected applying several filters. At least one hit on the TW and one track in the VTX detector have to be reconstructed. If more than one vertex is found in the VTX detector, the one closest to the position of the on-target BM track extrapolation is taken as the true vertex for the event under study, while the others are discarded as PU vertices. Only hits on the TW for which a charge assignment is possible are considered (see Sec. IV A). Only VTX tracks that are in the ALADIN magnet window entrance acceptance are considered.

(2) For all the preselected events an iterative scan of the matching between VTX tracks and TW hits is performed, producing a list of global track candidates. Each track from the VTX is paired with each hit from the TW: Clustering of TW hits is done afterwards, when the candidates are ranked and combined. For each candidate a minimization algorithm determines the optimal value of pc/Z and the corresponding trajectory that matches the VTX track before the magnet and the TW hit is found.

(3) The track candidates are finally combined and ranked in accordance with the VTX-TW matching quality. Duplicated tracks in which the same fragment has produced a hit in both the front and the rear TW walls are selected according to geometrical and energetic criteria and are properly combined. A scoring function to select the best candidates is then applied to the purged list. The resulting track list, in which each VTX track is used to build only one global track, is then used as input for the cross-section measurements.

The scoring algorithm combines the information from the VTX and the TW detectors to select the best track candidates. The quantities used to weigh each VTX-track–TW-hit pair are the difference between the VTX and TW Z_{ID} (Δ_{Chg}) and the difference between the y position as extrapolated from the VTX and as measured with the TW (Δ_y). The adopted scoring function is $\sqrt{\Delta^2_{\mathrm{Chg}} \mathrm{W}^2_{\mathrm{Chg}} + \Delta^2_Y y^2_{\mathrm{W}}}$. The $\mathrm{W}_{\mathrm{Chg}}$ and y_{W} weights have been optimized using the full MC simulation by minimizing the fraction of reconstructed tracks from combinatorial background.

An example of the scan performed to identify the best $\mathrm{W}_{\mathrm{Chg}}$ and y_{W} weights is shown in Fig. 13 for H and He fragments. Having set y_{W} to 1, the fraction of tracks in which the VTX track and the TW hits are not correctly paired with respect to the total number of reconstructed tracks is studied as a function of the charge weight $\mathrm{W}_{\mathrm{Chg}}$. The final $\mathrm{W}_{\mathrm{Chg}}$ value is identified looking at the plateau reached in Fig. 13 for the light fragments and considering that for fragments with Z greater than three, for large values of $\mathrm{W}_{\mathrm{Chg}}$, the combinatorial fraction increases (owing to the reduced discrimination power of the VTX detector). The final values of $\mathrm{W}_{\mathrm{Chg}}$ and y_{W} identified using the full scan on all the fragments are, respectively, $\mathrm{W}_{\mathrm{Chg}} = 8$ and $y_{\mathrm{W}} = 1$ (cm^{-1}).

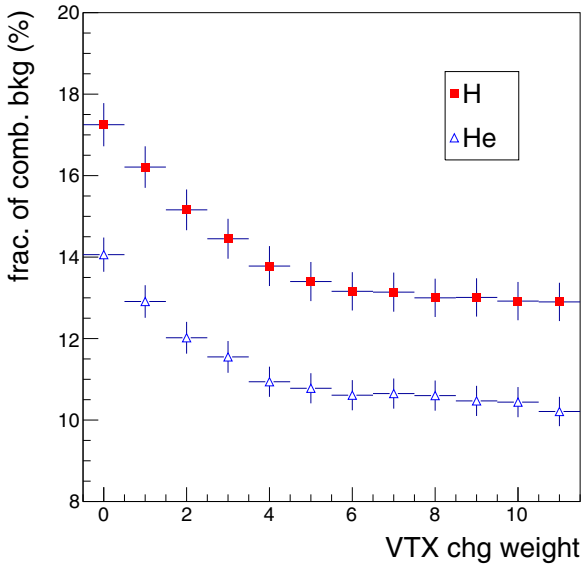

FIG. 13. Optimization of the W_{Chg} weight, based on the TW and VTX charge identification criteria, in the reconstruction. The fraction of tracks in which the VTX track and the TW hits are not correctly paired with respect to the total number of reconstructed tracks is shown as a function of W_{Chg}.

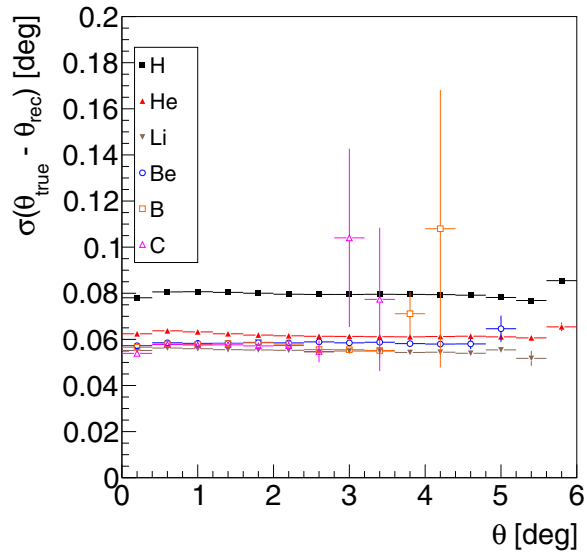

FIG. 14. Angular resolution as a function of the fragment polar angle.

For each selected global track candidate, all the measured quantities are computed: The charge and the TOF are measured by the TW (for details see Sec. IV A); the particle path (L) and the momentum over charge ratio (pc/Z) are determined by the tracking algorithm, allowing a measurement of the fragment speed [β defined as $L/(c \cdot \mathrm{TOF})$]; the mass is computed as $pc/(\gamma \cdot \beta)$. The quantities used to display the single differential cross sections (SDCS) spectra are respectively the fragment normalized kinetic energy (E_{kin}/nucleon), computed as the total fragment kinetic energy divided by the mass number, and the fragment production angle (θ) with respect to the ion incoming direction, measured using the tracks reconstructed by the BM and VTX detector.

C. Tracking algorithm performances

The global reconstruction algorithms have been benchmarked against the full MC simulation (see Sec. III). The angular and kinetic energy resolutions have been estimated to evaluate possible biases introduced by the reconstruction and to optimize the binning adopted for the SDCS measurement. The tracking efficiency and the background characterization have been studied using the full MC simulation as well.

1. Angular resolution

The angular resolution has been evaluated using global tracks from the full MC sample and it has been determined comparing the true fragment direction at the target exit point with the one reconstructed by the FIRST tracking algorithm. The resolution is found to be stable against the track angle, as shown in Fig. 14 with mean values that are in the range 0.06° (for helium ions up to borons) to 0.08° (for protons). Such numbers are entirely dominated by the intrinsic resolution of the VTX detector.

When comparing the reconstructed fragment direction with the generated value, computed inside the target, the resolution value is instead in the 0.1°–0.15° range, being completely dominated by the multiple scattering and depending on the fragment charge and energy.

2. Normalized kinetic-energy resolution

The kinetic-energy resolution ($\sigma_{E_{\mathrm{kin}}}$) has been evaluated using global tracks from the full MC sample. In the $\sigma_{E_{\mathrm{kin}}}$ distribution two main event categories can be identified: The events in which the tracks are built using the correct combinations of VTX track and TW hits and the events in which the VTX and TW candidates were not correctly paired. The reconstruction biases, as well as the resolutions, measured for the two categories are significantly different, as shown in Fig. 15 for H fragments.

The reconstruction efficiency and resolutions are estimated using the correctly paired tracks, while the wrongly paired combinations are used to model the combinatorial background as discussed in Sec. IV D.

Figure 16 shows the E_{kin}/nucleon resolution as a function of the measured normalized kinetic energy. The mass resolution, for the different fragment Z_{ID}, varies in the 0.05–0.2 (GeV/c^2) range for H fragments, increasing up to 0.3–0.5 (GeV/c^2) for carbon ions. The obtained resolution can be related to the measured TOF and momentum resolution using Eq. (1),

$$\frac{\Delta M}{M} = \sqrt{\left(\frac{\Delta p}{p}\right)^2 + \left(\gamma^2 \frac{\Delta \mathrm{TOF}}{\mathrm{TOF}}\right)^2}. \qquad (1)$$

The TOF resolution (800 ps), presented in Sec. II E 3, was mainly attributable to the aging of the scintillator using for the TW slats construction, the intercalibration, and remaining

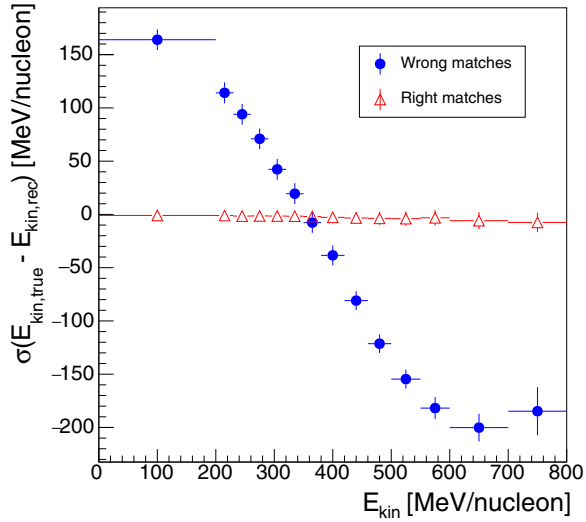

FIG. 15. Reconstruction biases (mean difference between generated and reconstructed values) in $E_{\rm kin}$/nucleon for H tracks with correct and wrong VTX/TW matches.

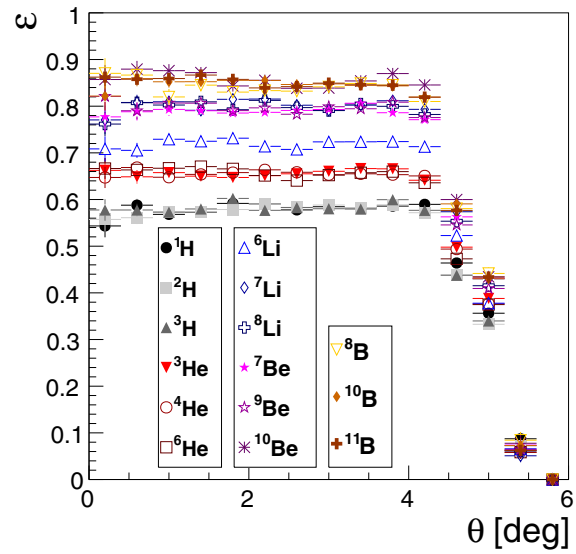

FIG. 17. Tracking efficiency ($\varepsilon_{\rm trk}$) as a function of fragment measured angle θ.

differences in the electronics readout of the 192 TW slats. The momentum resolution, instead, was dominated by the absence of a secondary tracker after the magnet. The MUSIC detector could not be operated during the data taking and the tracking algorithm had to use the information provided by the hits reconstructed in the TW, with a 0.8-cm spatial resolution along the x axis. For fixed TW spatial and temporal resolutions, the resolution on the reconstructed mass increases as a function of the fragment charge (as the tracking is sensitive to p/Z).

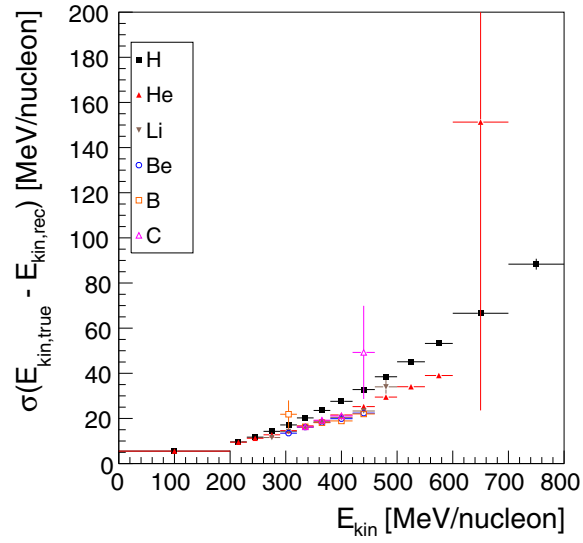

FIG. 16. $E_{\rm kin}$/nucleon resolution for fragments with different $Z_{\rm ID}$, from a global track MC sample selected requiring only correctly paired VTX tracks and TW hits.

3. Reconstruction efficiency

The reconstruction efficiency has been evaluated using the flat biased MC simulation sample (see Sec. III). The number ($n_{\rm prod}$) of reconstructible charged fragments is computed counting the fragments that emerge from the target region and point inside the geometrical acceptance of the ALADIN magnet. The number of reconstructed fragments ($n_{\rm rec}$) is computed counting the fragments in which the TW and VTX hits belonging to the same true MC track are used to build a reconstructed global track. The efficiency is hence defined as $\varepsilon_{\rm trk} = n_{\rm rec}/n_{\rm prod}$ and it is shown in Fig. 17 as a function of the measured angle θ for different isotopes. The uncertainties shown are statistical only.

The drop observed around 5° is attributable to the geometrical acceptance of the ALADIN magnet entrance window. The efficiency as a function of $E_{\rm kin}$/nucleon is nearly flat in the full energy range, with a significant drop only in the very first bin (below 200 MeV/nucleon).

The efficiency depends on several parameters and MC settings like the energy threshold implemented in the simulation of the TW signal channels response, the relative geometrical positioning of all the detectors and of the magnet and the detector dishomogeneities. To take into account the simulation setup-related impact on the measurement, a set of systematic studies has been performed and are documented in Sec. VI. In particular, the largest contribution to the systematic uncertainty on the efficiency measurement turned out to be the energy threshold implemented in the simulation of the TW response to the protons and light-ion signal (see, for example, Figs. 24(a) and 24(b), set of red points).

The tracking efficiency computed using the full unbiased MC sample has been used as a cross-check in the analysis to cite a systematic uncertainty as explained in Sec. VI.

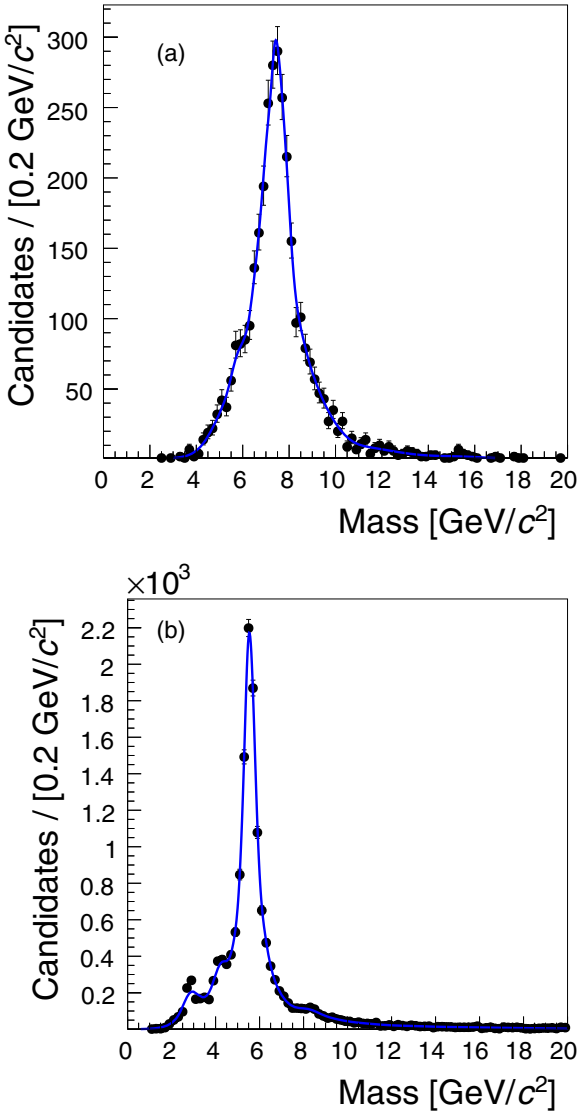

FIG. 18. Combinatorial background candidates invariant mass distribution in the full MC sample. (a) Mass distribution for Be candidates with $0.4^\circ < \theta < 0.8^\circ$. (b) Mass distribution for Li candidates with kinetic energy in the 350–380 MeV/nucleon range.

D. Combinatorial background evaluation

When pairing VTX tracks and TW hits, as described in Sec. IV B, one has to account for wrong matches or matching between background hits and/or fake tracks forming a random combination that is selected by the scoring algorithm. Such fragments are defined as a residual "combinatorial background," because they represent the result of a reconstruction that, after having applied the scoring algorithm, artificially combines tracks and hits not belonging to a true, common fragment.

The mass spectra of such candidates have to be determined and properly taken into account when measuring the fragment production yields. Figure 18 shows, for the full MC sample, the mass spectra for Be candidates with $0.4^\circ < \theta < 0.8^\circ$ (left) and for Li candidates with kinetic energy in the 350–380 MeV/nucleon range (right). Combinatorial background candidates were selected by requiring, at MC truth level, that the VTX tracks and the TW hits used to build the track belong to two different particles.

In Fig. 18, the probability density function (PDF) used to model the combinatorial background in the unbinned likelihood fits is shown as a blue curve superimposed to the reconstructed mass spectra (black dots). The PDF is built from the MC spectra using the one-dimensional kernel estimation method [28] (ROOKEYSPDF) provided by the ROOFIT package [29].

The uncertainties related to the modeling of the combinatorial background mass spectra have to be taken into account when fitting the data distributions: The systematic uncertainty affecting the cross-section measurement is discussed in Sec. VI.

E. Cross-feed evaluation

The limited precision of the Z_{ID} algorithm described in Sec. IV A implies that some fragments are identified with a wrong charge, biasing the final cross-section measurement. To properly correct for the cross feed between fully reconstructed fragments, a method based on the full MC sample information has been developed.

The effect owing to the wrong Z_{ID} reconstruction is shown clearly in Fig. 19, where the reconstructed mass spectrum is shown for fragments in which $Z_{\mathrm{ID}}^{\mathrm{rec}}$ is equal to 3. The total spectrum is shown in black (solid line). The contribution from the combinatorial background (see Sec. IV D) is shown in

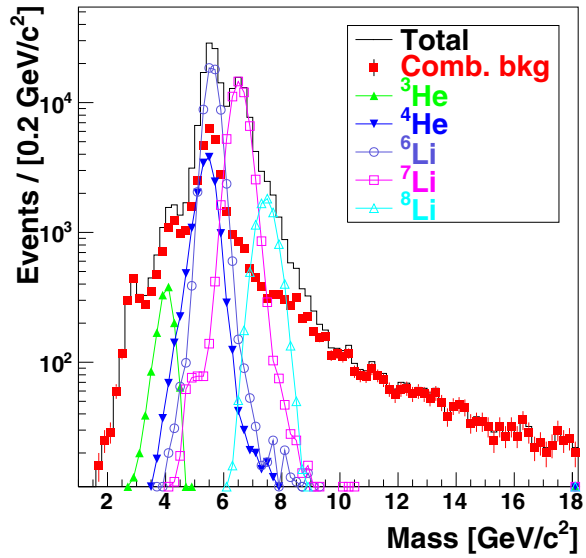

FIG. 19. Reconstructed mass spectrum for Li fragments using the full MC simulation sample. The black line is the total reconstructed spectrum. The red solid squares show the combinatorial background contamination. The main signal contributions to the spectrum, respectively from ^{6}Li, ^{7}Li, and ^{8}Li, are shown as open symbols (circles, squares, and triangles, respectively). The cross-feed background from ^{3}He and ^{4}He is shown by solid triangles (green and blue, respectively).

red solid squares, while the main signal contributions to the spectrum, respectively from ^{6}Li, ^{7}Li, and ^{8}Li, are shown as open symbols (circles, squares, and triangles, respectively). A clear contamination from ^{4}He appears (in blue solid triangles), under the ^{6}Li peak: Such contamination cannot be distinguished by the mass fit machinery (the slight shift in central mass values between ^{4}He and ^{6}Li peaks cannot be used in data owing to the limited mass resolution) and hence has to be properly subtracted from the fitted number of reconstructed fragments.

To compute the correction factors ε_i^{xf} that have to be applied to the $Y_i^{\rm raw}$ reconstructed yields for each isotope, we have analyzed the full MC sample in bins of reconstructed angle and kinetic energy and computed the contaminations relative to signal and cross-feed isotopes that have nearly the same mass shape. While the absolute amount of a given contamination under a certain reconstructed peak depends clearly on the absolute fragmentation cross section implemented in the MC, the cross-feed contamination is a relative correction that depends on the capability of the MC simulation to reproduce the ratio between the different cross sections.

We have therefore corrected the ε_i^{xf} factors to take into account the difference in ratio of the integrated cross sections between data and MC: The change in each isotope total cross section measured without any correction has been used to assign a systematic uncertainty (see Sec. VI).

F. Kinetic-energy distribution unfolding

The resolution studies discussed in Sec. IV C and presented in Fig. 16 showed that the kinetic-energy resolution degrades, as expected, with the fragment kinetic energy. To correct the measured energy for this resolution effect, whose main impact on the result is to broaden the kinetic-energy distribution, and to gain access to the true production kinetic energy of the fragment, an unfolding procedure has been setup using the ROOUNFOLD [30] toolkit package developed using the ROOT framework [31].

The access to the true production $E_{\rm kin}$/nucleon is particularly important when applying the tracking efficiency corrections [see Sec. V, Eqs. (2) and (3)] to the measured yields, because these corrections are determined as a function of the true production energy. A biased MC simulation has been used for this purpose: A sample of 10^7 events for each isotope has been generated with FLUKA producing directly from the target fragments with a flat production $E_{\rm kin}$/nucleon spectrum in the range 0–800 MeV/nucleon. Using the MC simulation it is possible to build the two-dimensional unfolding matrix that holds the information needed to correlate the reconstructed kinetic energy with the energy used at generator level. The details on the unfolding algorithm are given elsewhere [32].

For the application to FIRST, we used a Bayesian unfolding method with regularization strength (iterations number) τ optimized on the full MC samples by minimizing the χ^2 between the unfolded (measured) spectrum and the true (generated) one.

V. CROSS-SECTION MEASUREMENTS

The fragment production single differential cross sections, as functions of the normalized kinetic energy (E) or angle with respect to the ion incoming direction (θ), are defined as

$$\frac{d\sigma_i}{d\theta} = \frac{Y_i(\theta)}{N_{^{12}\rm C} \times N_{\rm t,S} \times \Omega(\text{ph.sp.}) \times \epsilon_{\rm trk}(\theta)}, \tag{2}$$

$$\frac{d\sigma_i}{dE} = \frac{Y_i(E)}{N_{^{12}\rm C} \times N_{\rm t,S} \times \Omega(\text{ph.sp.}) \times \epsilon_{\rm trk}(E)}, \tag{3}$$

where $Y_i(E,\theta)$ are the number of reconstructed fragments with a given atomic and mass number, $N_{\rm t,S}$ is the number of particles in the target per unit surface, $N_{^{12}\rm C}$ is the number of ^{12}C ions impinging on the target, $\epsilon_{\rm trk}$ is the tracking reconstruction efficiency (defined in Sec. IV C 3) and Ω(ph.sp.) is the phase space of the angular (θ) or kinetic energy (E) bin.

The number of target particles per unit surface is given by $N_{\rm t,S} = (\rho_{\rm tgt} \times {\rm th} \times N_A)/A$ where the $\rho_{\rm tgt} \times$ th, the product of the target density and the target thickness (th), was measured to be 0.96 ± 0.01 g/cm^2, and N_A and A are the Avogadro number and the gold atomic mass, respectively.

The phase space factor [Ω(ph.sp.)] is defined, according to the angular ($BW_\theta = \theta_{\rm max} - \theta_{\rm min}$) and kinetic-energy range ($BW_E = E_{\rm max} - E_{\rm min}$) of the selected fragments, as either $2\pi[\cos(\theta_{\rm min}) - \cos(\theta_{\rm max})]$ or $(E_{\rm max} - E_{\rm min})$ for SDCS as a function of the polar angle or kinetic energy, respectively. The size of BW_E and BW_θ bin widths used for the cross-section measurements have been chosen to limit the migrations between the different bins.

The number of ^{12}C ions impinging on the target ($N_{^{12}\rm C}$) is given by counting the physics unbiased triggers (see Sec. II F). The occurrence of multiple ^{12}C ions in a single event has been measured and found to be negligible in the data sample: For each trigger a single ^{12}C ion crossing is counted.

While the charge of each fragment is reconstructed using either the VTX or the TW detector, the production abundance of each fragment ($Y_i^{\rm raw}$), as well as the identification of different isotopes for each charge hypothesis is measured using the reconstructed mass spectra.

The $Y_i^{\rm raw}$yields are measured using an extended unbinned maximum likelihood fit, performed using the ROOFIT [29] toolkit. An example of such fits, for fragments of different charges and selected in different $E_{\rm kin}$/nucleon and θ ranges, is shown in Figs. 20 and 21. The top row shows the invariant mass fits to the H fragment spectra in a given bin of angle (left) and energy (right), while the bottom row shows the same information for Li fragments in different angle (left) and energy (right) bins. Superimposed to the data distribution (black dots), the total PDF is shown (in red), while the signal PDF, modeling the various isotopes, is shown in blue. A magenta dotted line shows the contribution from the combinatorial background.

To model the signal PDFs in a given energy or angular bin, we use one Gaussian for each isotope, accounting for the most abundant species. In the case of beryllium fragments a single Gaussian was used to model ^{9}Be and ^{10}Be isotopes to improve the fit stability and the background subtraction, measuring the total number of ^{9,10}Be fragments. The background PDF,

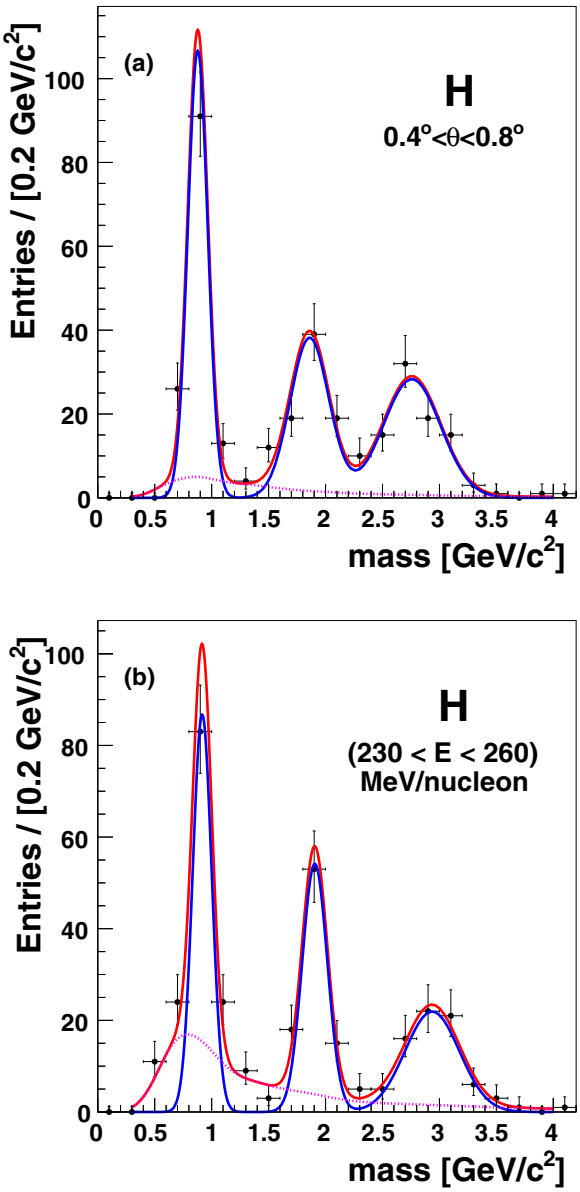

FIG. 20. Fit results for H fragments mass spectra in different E, θ ranges. (a) Invariant mass fits for H fragments with polar angles between 0.4° and 0.8°. In (b) fragments with the same atomic number and a normalized kinetic energy in the range between 230 and 260 MeV/nucleon are shown. Superimposed to the data distribution (black dots), the total PDF is shown (in red), while the signal PDF, modeling the various isotopes, is shown in blue. A magenta dotted line shows the contribution from the combinatorial background.

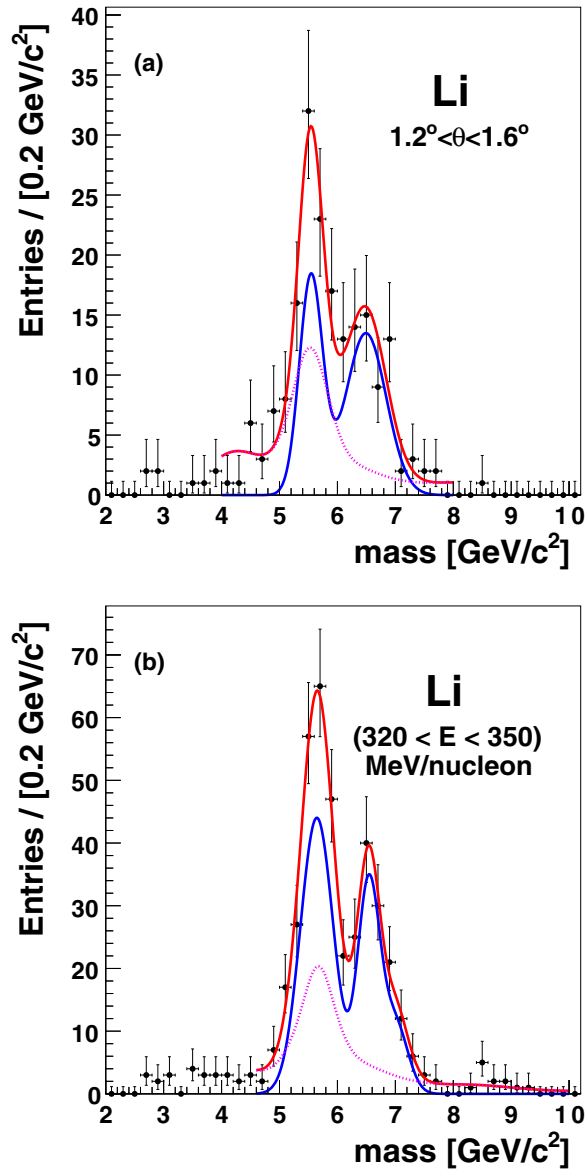

FIG. 21. Fit results for Li fragments mass spectra in different E, θ ranges. (a) Invariant mass fits for Li fragments with polar angles between 1.2° and 1.6°. In (b) fragments with the same atomic number and a normalized kinetic energy in the range between 320 MeV/nucleon and 350 MeV/nucleon are shown. Superimposed to the data distribution (black dots), the total PDF is shown (in red) while the signal PDF, modeling the various isotopes, is shown in blue. A magenta dotted line shows the contribution from the combinatorial background.

that is, accounting for the combinatorial background, has been described in Sec. IV D and shown in Fig. 18.

The Y_i^{raw}yields from the fit have yet to be corrected for the cross-feed contamination (see Sec. IV E). The yields used for the cross-section calculation are determined as $Y_i = \varepsilon_i^{xf} \times Y_i^{\text{raw}}$.

The yields to be used in the SDCS measurement as a function of E_{kin} are then corrected for the kinetic-energy resolution effect, as described in Sec. IV F. The *unfolded* yields are the ones used for the SDCS calculation.

The SDCS measurement procedure was validated using the MC simulation, looking for possible biases introduced by the reconstruction strategy and algorithms: The events from the simulation sample have been processed with the reconstruction software and the production cross section obtained for each isotope (σ_{rec}) have been compared with the values implemented at generator level (σ_{tru}). The difference between the measured values has been found to be consistent with zero within the total uncertainty in all cases, and hence

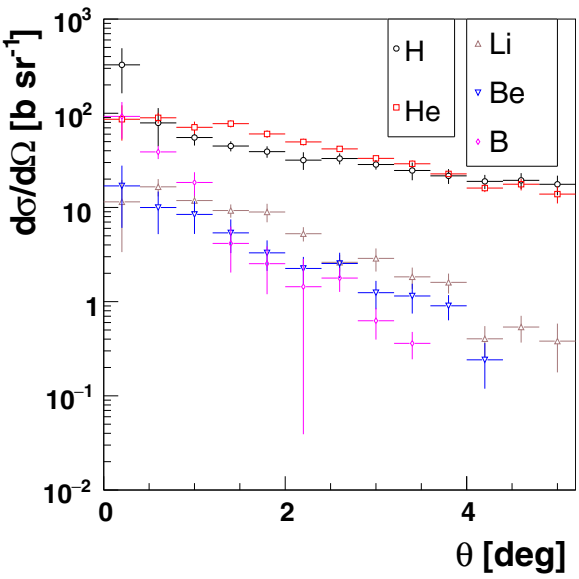

FIG. 22. SDCS of different charge (Z) fragment production, as a function of the fragment angle with respect to the ion incoming direction, measured using Eq. (2). The total uncertainty (stat. and syst. added in quadrature) is shown.

no correction has been applied to the measured cross sections on the data sample.

The measured SDCS as a function of θ and $E_{\rm kin}$ are shown respectively in Figs. 22 and 23. The uncertainty shown in the plot is the total uncertainty and accounts also for the systematic contribution, evaluated as described in Sec. VI. The $E_{\rm kin}$ results are shown for fragments in the ALADIN acceptance ($\lesssim 6^\circ$).

The histograms for each atomic number have been obtained by summing up all the non-negligible contributions from different isotopes that have the same $Z_{\rm ID}$. A discussion of the

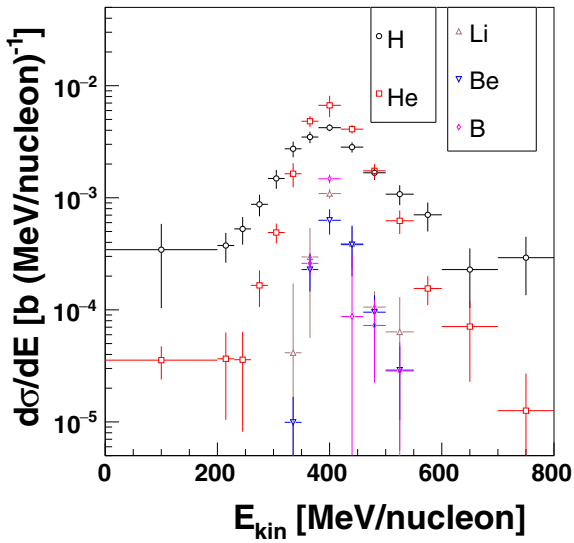

FIG. 23. SDCS of different charge (Z) fragment production, as a function of the fragment normalized kinetic energy, measured using Eq. (3) for fragments within the ALADIN angular acceptance ($\lesssim 6^\circ$). The total uncertainty (stat. and syst. added in quadrature) is shown.

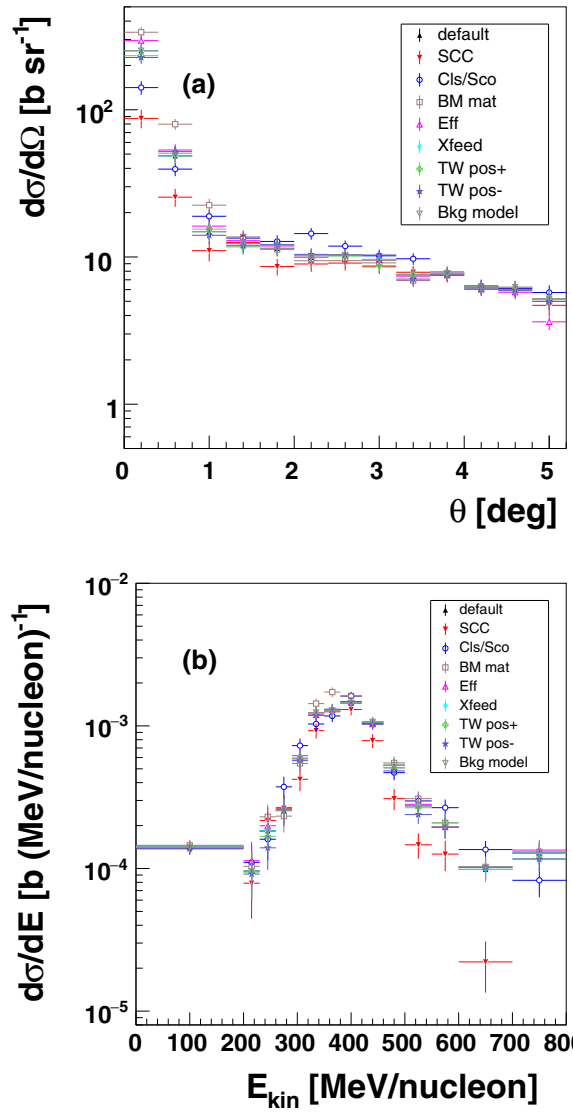

FIG. 24. Effect of systematic checks on the production cross sections of ^{2}H fragments. The angular (a) and kinetic-energy distributions (b) are shown. The production cross sections obtained changing the analysis strategy, algorithm, and cuts are shown. The details on the different spectra labels can be found in the text.

systematic uncertainties affecting the results is presented in the following section and shown, for ^{2}H fragments, in Fig. 24. A full set of tables and plots for all the detected isotopes is provided in the Appendix: the cross sections are reported in detail in Tables I, II, III, and IV and shown in Figs. 25 and 26.

VI. SYSTEMATIC CHECKS

Several systematic checks have been performed to assess the impact of the detector resolution and discrepancies between data and MC on the SDCS measurements. The analysis has been repeated several times, changing the reconstruction algorithms, MC samples, and measurement strategies: The systematic uncertainty relative to each measurement has been assigned by assessing the spread of the results (semidispersion).

TABLE I. Single differential cross sections (b sr^{-1}) as a function of the polar angle θ. The halved bin size is shown in parentheses ( ) in the first column. The total uncertainty (stat. and syst. added in quadrature) is shown in parentheses ( ) beside the measured value. The shown values refer to the main isotopes of the hydrogen and helium fragment species.

θ (deg)	^{1}H $d\sigma/d\Omega$ (b sr^{-1})	^{2}H $d\sigma/d\Omega$ (b sr^{-1})	^{3}H $d\sigma/d\Omega$ (b sr^{-1})	^{3}He $d\sigma/d\Omega$ (b sr^{-1})	^{4}He $d\sigma/d\Omega$ (b sr^{-1})
0.2(0.2)	41 (15)	2.5 10^{2} (1.3 10^{2})	33 (11)	13 (15)	74 (30)
0.6(0.2)	12 (3.4)	49 (28)	18 (4.4)	12 (4.1)	78 (11)
1(0.2)	24 (2.9)	15 (6)	16 (3.5)	12 (3.2)	59 (7.5)
1.4(0.2)	20 (2.4)	12 (1.7)	12 (3.2)	12 (2)	65 (6.8)
1.8(0.2)	17 (1.8)	11 (2.4)	10 (2.1)	11 (1.7)	50 (4.8)
2.2(0.2)	15 (2.6)	9.9 (2.9)	7.2 (1.7)	7.9 (1.7)	42 (3.9)
2.6(0.2)	16 (2.3)	10 (1.7)	6.8 (0.89)	8.1 (0.94)	34 (2.6)
3(0.2)	14 (1.7)	9.6 (1.3)	4.5 (0.76)	8.1 (0.98)	25 (2.1)
3.4(0.2)	13 (2.6)	7.6 (1.6)	3.9 (0.65)	9.2 (1.3)	20 (1.7)
3.8(0.2)	10 (1.3)	7.7 (0.75)	3.8 (0.69)	7.5 (0.71)	15 (1.3)
4.2(0.2)	9.6 (1.3)	6.3 (0.63)	3.1 (0.58)	4.7 (0.79)	11 (0.99)
4.6(0.2)	10 (1.7)	6.2 (0.7)	2.9 (0.7)	4.2 (1.7)	13 (1.5)
5(0.2)	9.3 (2.3)	5.2 (1.2)	3.2 (0.77)	6 (1.8)	7.8 (2.2)

In the following we refer to the result obtained by following the prescriptions and strategies outlined in the previous sections as the *default* result.

An important contribution to the systematic uncertainty quoted for the production cross section of H fragments comes from the modeling of the TW hit detection efficiencies. In the TW detector, designed to have a wide dynamic range to detect heavy Z fragments, the H fragment signals are close to the minimum threshold needed to have a signal in the CFDs. For this reason, the events in which only one TDC gives a signal when a slat is hit are used to improve the efficiency for low-charge fragments.

To evaluate the impact of the threshold modeling in our MC simulation, the analysis has been repeated, rejecting the events in which only one TDC per slat gave a signal: The change with respect to the *default* is a measurement of the goodness of the MC simulation of our thresholds and the relative hit reconstruction efficiency. The difference observed is, as expected, significant only for H fragments and is shown, in red full topside-down triangles in Fig. 24 (SCC spectrum).

The analysis has also been redone by changing both the scoring function, using different weights, and disabling the TW hits clustering algorithm. The weights used for the systematic checks were alternatively the set $W_{Chg} = 8$, $y_W = 0$ (cm^{-1}), the set $W_{Chg} = 0$ and $y_W = 1$ (cm^{-1}), and the set $W_{Chg} = 6$ and $y_W = 1$ (cm^{-1}) to test the impact of a charge-based and y-matching-only strategy and the impact of the choice of the best weight pair. The results for ^{2}H fragments, taking the largest observed difference, are shown in Fig. 24 (Cls/Sco spectra).

The VTX tracking robustness and the matching of BM and VTX information has been checked by changing the reconstruction algorithms relaxing the requirement of having

TABLE II. Single differential cross sections (b sr^{-1}) as a function of the polar angle θ. The halved bin size is shown in parentheses ( ) in the first column. The total uncertainty (stat. and syst. added in quadrature) is shown in parentheses ( ) beside the measured value. The shown values refer to the main isotopes of the lithium, beryllium, and boron fragment species. ^{9}Be and ^{10}Be are shown together as measured by the mass fit and explained in Sec. V.

θ (deg)	^{6}Li $d\sigma/d\Omega$ (b sr^{-1})	^{7}Li $d\sigma/d\Omega$ (b sr^{-1})	^{7}Be $d\sigma/d\Omega$ (b sr^{-1})	^{9,10}Be $d\sigma/d\Omega$ (b sr^{-1})	^{10}B $d\sigma/d\Omega$ (b sr^{-1})	^{11}B $d\sigma/d\Omega$ (b sr^{-1})
0.2(0.2)	5.5 (7.8)	6 (4.7)	5 (6.1)	12 (8.5)	79 (27)	14 (24)
0.6(0.2)	11 (2.7)	5.8 (1.6)	3.8 (2.7)	6.1 (2.9)	24 (3.4)	15 (5.5)
1(0.2)	3.4 (1.4)	8.5 (2.3)	4.5 (2)	3.9 (1.3)	6.2 (2.8)	12 (4.6)
1.4(0.2)	3.2 (1.1)	6.1 (1.1)	3.4 (1.5)	1.9 (0.76)	2.5 (1.6)	1.7 (2.2)
1.8(0.2)	4.8 (1.7)	4.1 (0.69)	1.9 (0.77)	1.4 (0.59)	2 (1.3)	0.51 (0.67)
2.2(0.2)	2.4 (0.6)	2.9 (0.7)	1.6 (0.54)	0.65 (0.28)	0.63 (0.97)	0.81 (0.75)
2.6(0.2)	0.91 (0.4)	1.7 (0.44)	1.9 (0.56)	0.69 (0.31)	1.1 (0.42)	0.67 (0.32)
3(0.2)	1.7 (0.73)	1.2 (0.32)	1.1 (0.28)	0.16 (0.21)	0.41 (0.18)	0.22 (0.19)
3.4(0.2)	1.1 (0.37)	0.74 (0.26)	0.89 (0.28)	0.26 (0.16)	0.098 (0.071)	0.26 (0.11)
3.8(0.2)	1.4 (0.45)	0.19 (0.35)	0.72 (0.21)	0.19 (0.1)		
4.2(0.2)	0.3 (0.18)	0.1 (0.23)	0.23 (0.11)	0.0076 (0.038)		
4.6(0.2)	0.41 (0.18)	0.13 (0.16)				
5(0.2)	0.34 (0.16)	0.046 (0.099)				

TABLE III. Single differential cross sections (b nucleon/MeV) as a function of the normalized kinetic energy for fragments within the ALADIN angular acceptance ($\lesssim 6^\circ$). The halved bin size is shown in parentheses ( ) in the first column. The total uncertainty (stat. and syst. added in quadrature) is shown in parentheses ( ) beside the measured value. The shown values refer to the main isotopes of the hydrogen and helium fragment species.

Energy (MeV/nucl.)	^{1}H $d\sigma/dE$ (b nucl./MeV)	^{2}H $d\sigma/dE$ (b nucl./MeV)	^{3}H $d\sigma/dE$ (b nucl./MeV)	^{3}He $d\sigma/dE$ (b nucl./MeV)	^{4}He $d\sigma/dE$ (b nucl./MeV)
100(100)	1.58×10^{-4} (6.35×10^{-5})	1.42×10^{-4} (1.36×10^{-5})	4.45×10^{-5} (1.02×10^{-5})	2.47×10^{-5} (6.60×10^{-6})	1.09×10^{-5} (4.79×10^{-6})
215(15)	2.12×10^{-4} (7.64×10^{-5})	9.60×10^{-5} (3.86×10^{-5})	6.69×10^{-5} (2.77×10^{-5})	2.01×10^{-5} (1.84×10^{-5})	1.65×10^{-5} (1.36×10^{-5})
245(15)	3.12×10^{-4} (1.32×10^{-4})	1.84×10^{-4} (6.50×10^{-5})	3.18×10^{-5} (4.55×10^{-5})	2.22×10^{-5} (1.90×10^{-5})	1.37×10^{-5} (1.21×10^{-5})
275(15)	3.30×10^{-4} (9.42×10^{-5})	2.55×10^{-4} (9.00×10^{-5})	2.89×10^{-4} (5.72×10^{-5})	1.13×10^{-4} (4.81×10^{-5})	5.21×10^{-5} (2.28×10^{-5})
305(15)	5.91×10^{-4} (1.26×10^{-4})	5.89×10^{-4} (1.72×10^{-4})	3.07×10^{-4} (7.49×10^{-5})	2.11×10^{-4} (5.57×10^{-5})	2.79×10^{-4} (6.13×10^{-5})
335(15)	8.68×10^{-4} (1.32×10^{-4})	1.24×10^{-3} (2.79×10^{-4})	6.30×10^{-4} (1.57×10^{-4})	3.84×10^{-4} (1.02×10^{-4})	1.25×10^{-3} (2.50×10^{-4})
365(15)	1.39×10^{-3} (1.32×10^{-4})	1.28×10^{-3} (2.99×10^{-4})	8.09×10^{-4} (1.52×10^{-4})	8.84×10^{-4} (2.54×10^{-4})	3.94×10^{-3} (4.76×10^{-4})
400(20)	1.60×10^{-3} (1.46×10^{-4})	1.44×10^{-3} (1.91×10^{-4})	1.18×10^{-3} (1.39×10^{-4})	1.04×10^{-3} (5.44×10^{-4})	5.65×10^{-3} (8.09×10^{-4})
440(20)	1.13×10^{-3} (9.93×10^{-5})	1.06×10^{-3} (1.66×10^{-4})	6.41×10^{-4} (1.11×10^{-4})	7.76×10^{-4} (1.43×10^{-4})	3.32×10^{-3} (3.27×10^{-4})
480(20)	8.59×10^{-4} (9.48×10^{-5})	5.30×10^{-4} (1.34×10^{-4})	2.83×10^{-4} (7.02×10^{-5})	4.15×10^{-4} (1.38×10^{-4})	1.33×10^{-3} (2.46×10^{-4})
525(25)	6.14×10^{-4} (1.22×10^{-4})	2.75×10^{-4} (8.90×10^{-5})	1.89×10^{-4} (4.92×10^{-5})	1.74×10^{-4} (3.20×10^{-5})	4.49×10^{-4} (1.37×10^{-4})
575(25)	3.75×10^{-4} (8.74×10^{-5})	1.95×10^{-4} (7.73×10^{-5})	1.35×10^{-4} (5.69×10^{-5})	7.11×10^{-5} (6.00×10^{-5})	8.40×10^{-5} (5.21×10^{-5})
650(50)	8.73×10^{-5} (3.81×10^{-5})	9.86×10^{-5} (5.95×10^{-5})	4.29×10^{-5} (3.75×10^{-5})	7.00×10^{-5} (4.80×10^{-5})	8.45×10^{-7} (1.09×10^{-6})
750(50)	2.64×10^{-4} (7.46×10^{-5})	1.28×10^{-4} (6.89×10^{-5})	4.00×10^{-5} (2.36×10^{-5})	1.37×10^{-5} (1.36×10^{-5})	1.02×10^{-7} (4.83×10^{-7})

a BM matched track: The results are shown in Fig. 24 as *BM mat* values. The observed variations, in most bins, are within the statistical uncertainty.

To evaluate the impact on the limited precision of the TW position with respect to the general FIRST reference frame, the TW position in the reconstruction algorithm was changed by ±1 cm, corresponding to the resolution of the survey performed after the data taking. The result is shown in Fig. 24, labeled as TW pos+(−).

The differences in the mass spectra between data and MC have to be taken into account in the $Y_i^{\rm raw}$ measurement, to avoid any bias in the fit result. The mass fit study has been repeated after changing the ROOKEYSPDFsmoothing parameter (ρ) to test different descriptions of the peaking components in the observed mass distributions. The obtained result is, for most bins, well within the statistical uncertainty, as shown in Fig. 24 (spectrum labeled Bkg model).

It has also to be noted that the different analyses strategies used for the evaluation of the systematic uncertainty explored several combinatorial background conditions (modified shapes and different background contamination): The final systematic uncertainty therefore covers also the background contamination subtraction under different background conditions.

The systematic checks include the evaluation of the MC simulation impact on the estimate of the cross feed correction that is used to correct the $Y_i^{\rm raw}$ yields described in Sec. IV E. The data/MC difference rescaling used for the evaluation of the correction factors has been switched off to evaluate the maximum impact of this rescaling (spectrum labeled Xfeed in Fig. 24).

Finally, the differences in the tracking reconstruction efficiency computed as described in Sec. IV C 3 with the full unbiased MC sample have been taken into account when producing the spectrum labeled Eff in Fig. 24.

TABLE IV. Single differential cross sections (b nucleon/MeV) as a function of the normalized kinetic energy for fragments within the ALADIN angular acceptance ($\lesssim 6^\circ$). The halved bin size is shown in parentheses ( ) in the first column. The total uncertainty (stat. and syst. added in quadrature) is shown in parentheses ( ) beside the measured value. The shown values refer to the main isotopes of the lithium, beryllium, and boron fragment species. ^{9}Be and ^{10}Be are shown together as measured by the mass fit and explained in Sec. V.

Energy (MeV/nu.)	^{6}Li $d\sigma/dE$ (b nu./MeV)	^{7}Li $d\sigma/dE$ (b nu./MeV)	^{7}Be $d\sigma/dE$ (b nu./MeV)	^{9,10}Be $d\sigma/dE$ (b nu./MeV)	^{10}B $d\sigma/dE$ (b nu./MeV)	^{11}B $d\sigma/dE$ (b nu./MeV)
305(15)	3.79×10^{-7} (3.59×10^{-6})	4.30×10^{-6} (5.47×10^{-6})				
335(15)	6.88×10^{-6} (9.20×10^{-6})	3.45×10^{-5} (1.05×10^{-4})	9.89×10^{-6} (6.82×10^{-6})	2.73×10^{-8} (1.64×10^{-7})	7.59×10^{-8} (1.97×10^{-7})	
365(15)	1.68×10^{-4} (8.64×10^{-5})	1.28×10^{-4} (2.00×10^{-4})	1.49×10^{-4} (4.40×10^{-5})	8.01×10^{-5} (5.04×10^{-5})	1.99×10^{-4} (7.98×10^{-5})	6.12×10^{-5} (8.40×10^{-5})
400(20)	6.33×10^{-4} (1.43×10^{-4})	4.57×10^{-4} (8.42×10^{-5})	3.29×10^{-4} (1.47×10^{-4})	3.01×10^{-4} (8.15×10^{-5})	7.20×10^{-4} (2.79×10^{-4})	7.58×10^{-4} (2.62×10^{-4})
440(20)	1.43×10^{-4} (6.59×10^{-5})	2.48×10^{-4} (2.16×10^{-4})	2.52×10^{-4} (1.95×10^{-4})	1.30×10^{-4} (4.40×10^{-5})	2.37×10^{-5} (2.72×10^{-5})	6.34×10^{-5} (2.03×10^{-4})
480(20)	5.82×10^{-5} (3.33×10^{-5})	4.76×10^{-5} (2.61×10^{-5})	8.10×10^{-5} (3.01×10^{-5})	1.42×10^{-5} (3.45×10^{-5})	1.19×10^{-5} (4.70×10^{-5})	6.07×10^{-5} (4.78×10^{-5})
525(25)	6.25×10^{-5} (3.59×10^{-5})	1.04×10^{-6} (2.33×10^{-6})	1.81×10^{-5} (1.27×10^{-5})	1.09×10^{-5} (8.97×10^{-6})	7.77×10^{-6} (2.63×10^{-5})	2.07×10^{-5} (1.42×10^{-5})
575(25)	3.89×10^{-6} (1.06×10^{-5})	1.96×10^{-8} (1.05×10^{-7})	3.20×10^{-8} (3.61×10^{-8})	8.30×10^{-8} (9.08×10^{-8})	1.30×10^{-8} (5.72×10^{-7})	1.69×10^{-8} (2.37×10^{-8})

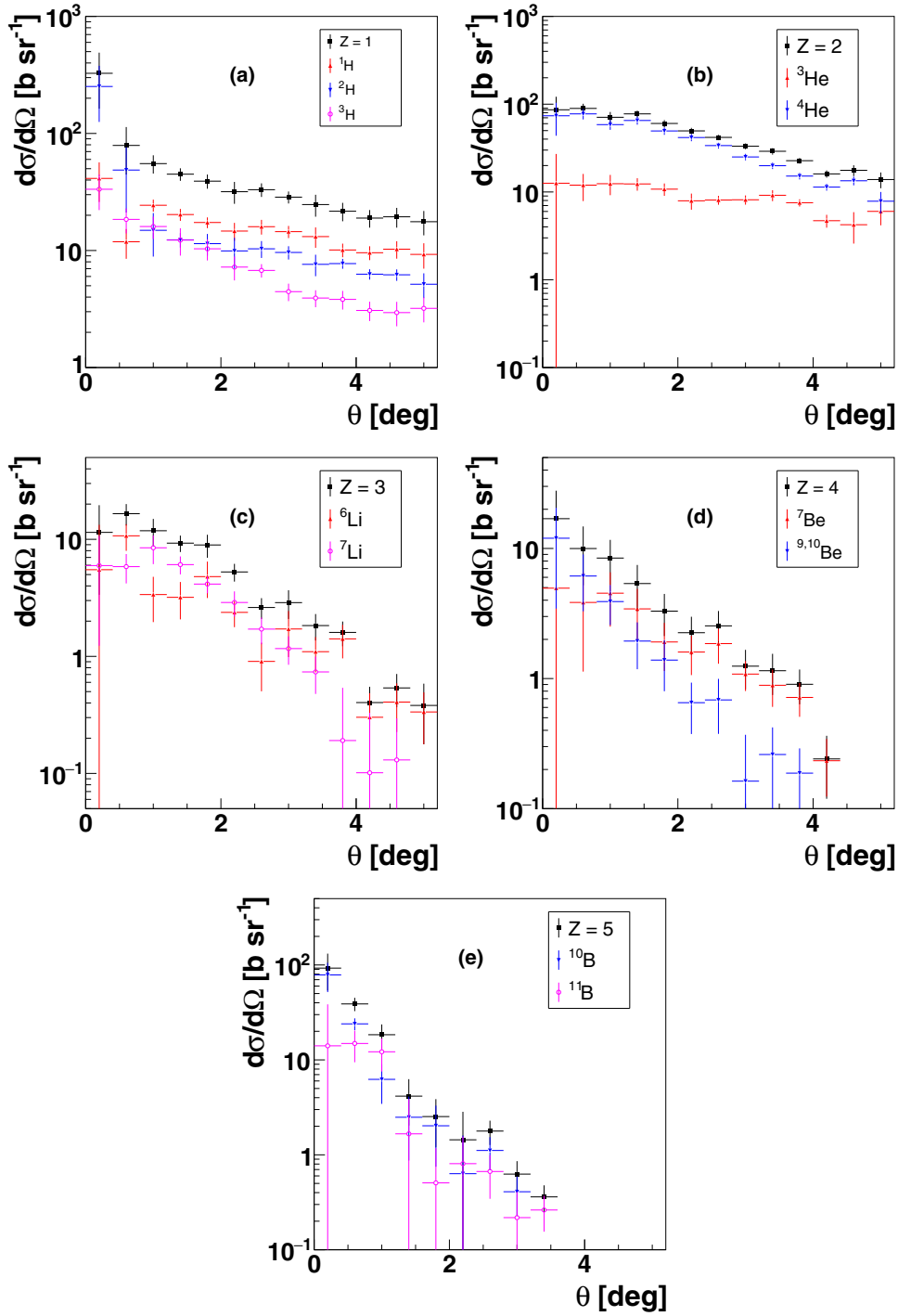

FIG. 25. SDCS of different charge (Z) fragment production as a function of the fragment angle with respect to the beam axis, computed using Eq. (2). The results for each isotope are shown separately, together with their sum (in black squares). ^{9}Be and ^{10}Be are shown together as measured by the mass fit and explained in Sec. V. The total uncertainty (stat. and syst. added in quadrature) is shown.

VII. CONCLUSIONS

The FIRST experiment performed a measurement of fragment production SDCS as a function of production angles and kinetic energies, studying a data sample of 4.5×10^{6} collisions of ^{12}C ions impinging on a thin (0.5 mm) gold target. The measurement experimental configuration, as well as the ^{12}C ion energy of 400 MeV/nucleon, made it possible to provide results that are particularly interesting for space applications.

The results presented here achieve an unprecedented precision on the single differential cross sections of carbon ions on a thin gold target.

This experimental input is highly valuable as it sets a reference point that will help the benchmarking of MC simulation

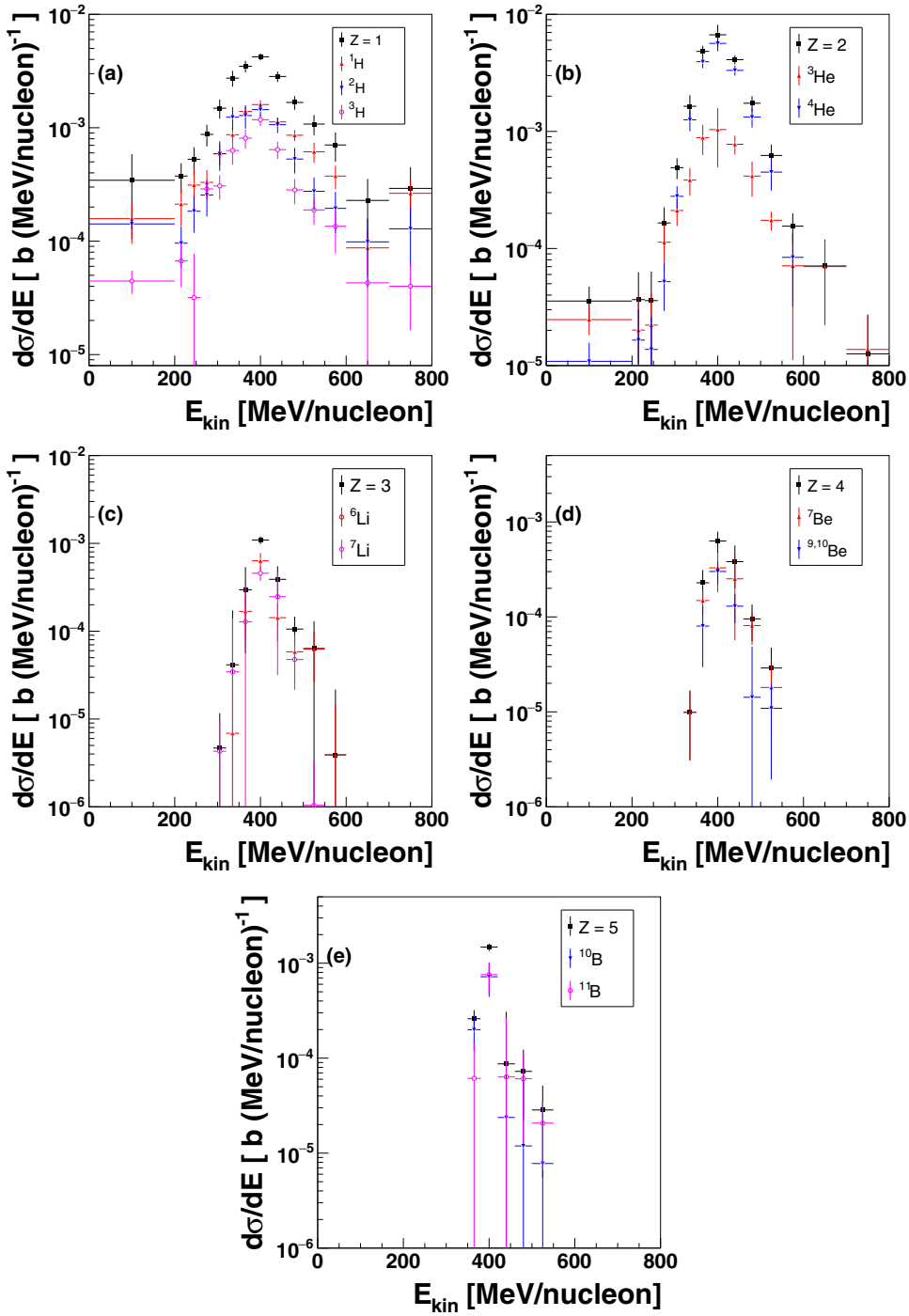

FIG. 26. SDCS of different charge (Z) fragment production, as a function of the fragment normalized kinetic energy, computed using Eq. (3) for fragments within the ALADIN angular acceptance ($\lesssim 6^{\circ}$). The results for each isotope are shown separately, together with their sum (in black squares). ^{9}Be and ^{10}Be are shown together as measured by the mass fit and explained in Sec. V. The total uncertainty (stat. and syst. added in quadrature) is shown.

software currently used for nuclear fragmentation studies for which a high precision is required and whose implications range from the space radiation to charged-particle-therapy applications.

ACKNOWLEDGMENTS

We would like to acknowledge M. Arba, L. La Delfa and M. Tuveri (INFN Sez. Cagliari), M. Anelli, S. Cerioni, G. Corradi, A. Mengucci, D. Riondino and R. Rosellini

(INFN, LNF), M. Capponi and A. Iaciofano (INFN, Sez. Roma3) for the technical design and mechanical work on the Interaction Region and Filippo Bosi (INFN Sez. Pisa) for his help and suggestions. We also acknowledge Dr. Håkan T. Johansson for the invaluable help in setting up the trigger. This work has been supported by the European Community FP7 - Capacities, contract ENSAR n^o 262010, and by FP7 - People, Contract No. PITNGA-2008-215840-PARTNER. This work was also supported by Junta de Andaluca and the Spanish Ministerio de Ciencia e Innovación Contracts No. P07-FQM-02894, No. FIS2008-04189, and No. FPA2008-04972-C03.

[1] M. Durante and F. A. Cucinotta, Physical basis of radiation protection in space travel, Rev. Mod. Phys. **83**, 1245 (2011).

[2] L. Ziwei, Determination of important nuclear fragmentation processes for human space radiation protection, Phys. Rev. C **75**, 034609 (2007).

[3] D. Schardt, T. Elsässer, and D. Schulz-Ertner, Heavy-ion tumor therapy: Physical and radiobiological benefits, Rev. Mod. Phys. **82**, 383 (2010).

[4] J. S. Loeffler and M. Durante, Charged particle therapy–optimization, challenges and future directions, Nat. Rev. Clin. Oncol. **10**, 411 (2013).

[5] T. Bohlen *et al.*, Benchmarking nuclear models of FLUKA and GEANT4 for carbon ion therapy, Phys. Med. Biol. **55**, 5833 (2010).

[6] J. W. Norbury, J. Miller, A. M. Adamczyk, L. Heilbronn, L. W. Townsend, S. R. Blattnig, and C. J. Zeitlin, Nuclear data for space radiation, Radiat. Meas. **47**, 315 (2012).

[7] N. Matsufuji *et al.*, Spatial fragment distribution from a therapeutic pencil-like carbon beam in water, Phys. Med. Biol. **50**, 3393 (2005).

[8] C. Zeitlin, S. Guetersloh, L. Heilbronn, J. Miller, A. Fukumura, Y. Iwata, and T. Murakami, Fragmentation cross sections of 290-MeV/nucleon and 400-MeV/nucleon C-12 beams on elemental targets, Phys. Rev. C **76**, 014911 (2007).

[9] T. Toshito *et al.*, Measurements of total and partial charge-changing cross sections for 200- to 400-MeV/nucleon C12 on water and polycarbonate, Phys. Rev. C **75**, 054606 (2007).

[10] C. Zeitlin, J. Miller, S. Guetersloh, L. Heilbronn, A. Fukumura, Y. Iwata, T. Murakami, S. Blattnig, R. Norman, and S. Mashnik, Fragmentation of ^{14}N, ^{16}O, ^{20}Ne, and ^{24}Mg nuclei at 290 to 1000 MeV/nucleon, Phys. Rev. C **83**, 034909 (2011).

[11] M. De Napoli *et al.*, Carbon fragmentation measurements and validation of the GEANT4 nuclear reaction models for hadrontherapy, Phys. Med. Biol. **57**, 7651 (2012).

[12] M. De Napoli *et al.*, Carbon fragmentation cross sections for hadrontherapy and space radiation protection, Nucl. Data Sheets **119**, 273 (2014).

[13] J. Dudouet, M. Labalme, D. Cussol, C. Finck, R. Rescigno, M. Rousseau, S. Salvador, and M. Vanstalle, Zero-degree measurements of ^{12}C fragmentation at 95 MeV/nucleon on thin targets, Phys. Rev. C **89**, 064615 (2014).

[14] J. Dudouet, D. Juliani, M. Labalme, D. Cussol, J. C. Angélique, B. Braunn, J. Colin, C. Finck, J. M. Fontbonne, H. Guérin, P. Henriquet, J. Krimmer, M. Rousseau, M. G. Saint-Laurent, and S. Salvador, Double-differential fragmentation cross-section measurements of 95 MeV/nucleon ^{12}C beams on thin targets for hadron therapy, Phys. Rev. C **88**, 024606 (2013).

[15] R. Pleskac *et al.*, The FIRST Experiment at GSI, Nucl. Instrum. Methods Phys. Res., Sect. A **678**, 130 (2012).

[16] http://www.iphc.cnrs.fr/-CMOS-ILC-.html.

[17] Ch. Hu-Guo *et al.*, First reticule size MAPS with digital output and integrated zero suppression for the EUDET-JRA1 beam telescope, Nucl. Instrum. Methods Phys. Res. **623**, 480 (2010).

[18] C. Sfienti *et al.*, Proceedings of the XLI International Winter Meeting on Nuclear Physics Bormio (Italy), Ricerca Scientifica ed Educazione Permamente Supplemento N. 120, p. 323 (2003).

[19] Z. Abou-Haidar *et al.*, Performance of upstream interaction region detectors for the FIRST experiment at GSI, J. Instrum. **7**, P02006 (2012).

[20] R. Rescigno *et al.*, Performance of the reconstruction algorithms of the FIRST experiment pixel sensors vertex detector, Nucl. Instrum. Methods Phys. Res., Sect. A **767**, 34 (2014).

[21] J. B. Birks, Scintillations from organic crystals: Specific fluorescence and relative response to different radiations, Proc. Phys. Soc. London, Sect. A **64**, 874 (1951).

[22] H. G. Essel and N. Kurz, The general purpose data acquisition system MBS, IEEE Trans. Nucl. Sci. **47**, 337 (2000).

[23] https://www.gsi.de/informationen/wti/ee/elekt_entwick lung/vulom_m_e.html.

[24] G. Battistoni *et al.*, The FLUKA code: Description and benchmarking, in *Proceedings of the Hadronic Shower Simulation Workshop, Fermilab 6–8 September 2006*, edited by M. Albrow and R. Raja, AIP Conf. Proc. No. 896 (AIP, New York, 2007), pp. 31–49.

[25] A. Ferrari, P. R. Sala, A. Fassò, and J. Ranft, FLUKA: A multi particle transport code, Tech. Rep. CERN-2005-10, INFN/TC05/11, SLAC-R-773, 2005.

[26] T. T. Böhlen, F. Cerutti, M. P. W. Chin, A. Fassò, A. Ferrari, P. G. Ortega, A. Mairani, P. R. Sala, G. Smirnov and V. Vlachoudis, The FLUKA code: Developments and challenges for high energy and medical applications, Nucl. Data Sheets **120**, 211 (2014).

[27] E. Spiriti *et al.*, The FIRST experiment: Interaction region and MAPS vertex detector, Nucl. Phys. B **215**, 157 (2011).

[28] K. S. Cranmer, Kernel estimation in high-energy physics, Comput. Phys. Commun. **136**, 198 (2001).

[29] W. Verkerke and D. P. Kirkby, The RooFit toolkit for data modeling, in *Proceedings of 2003 Conference for Computing in High-Energy and Nuclear Physics (CHEP 03), La Jolla, California, 24-28 Mar 2003*, eConf C0303241 (2003) MOLT007, arXiv:physics/0306116.

[30] T. Adye, in *Proceedings of the PHYSTAT 2011 Workshop on Statistical Issues Related to Discovery Claims in Search Experiments and Unfolding, CERN, Geneva, Switzerland, 17–20 January 2011*, edited by H. B. Prosper and L. Lyons, CERN-2011-006, pp. 313–318.

[31] R. Brun and F. Rademakers, ROOT-An object oriented data analysis framework, Nucl. Instrum. Methods Phys. Res., Sect. A **389**, 81 (1997).

[32] G. D'Agostini, A Multidimensional unfolding method based on Bayes' theorem, Nucl. Instrum. Methods Phys. Res., Sect. A **362**, 487 (1995).